A&A 427, 667–683 (2004)
DOI: 10.1051/0004-6361:20040504

Astronomy & Astrophysics

On the sizes of stellar X-ray coronae⋆

J.-U. Ness[1], M. Güdel[2], J. H. M. M. Schmitt[1], M. Audard[3], and A. Telleschi[2]

[1] Universität Hamburg, Gojenbergsweg 112, 21029 Hamburg, Germany
e-mail: jness@hs.uni-hamburg.de
[2] Paul Scherrer Institut, Würenlingen & Villingen, 5232 Villingen PSI, Switzerland
[3] Columbia Astrophysics Laboratory, 550 West 120th Street, New York, NY 10027, USA

Received 24 March 2004 / Accepted 5 July 2004

Abstract. Spatial information from stellar X-ray coronae cannot be assessed directly, but scaling laws from the solar corona make it possible to estimate sizes of stellar coronae from the physical parameters temperature and density. While coronal plasma temperatures have long been available, we concentrate on the newly available density measurements from line fluxes of X-ray lines measured for a large sample of stellar coronae with the Chandra and XMM-Newton gratings. We compiled a set of 64 grating spectra of 42 stellar coronae. Line counts of strong H-like and He-like ions and Fe XXI lines were measured with the CORA single-purpose line fitting tool by Ness & Wichmann (2002). Densities are estimated from He-like f/i flux ratios of O VII and Ne IX representing the cooler (1–6 MK) plasma components. The densities scatter between $\log n_e \approx 9.5$–11 from the O VII triplet and between $\log n_e \approx 10.5$–12 from the Ne IX triplet, but we caution that the latter triplet may be biased by contamination from Fe XIX and Fe XXI lines. We find that low-activity stars (as parameterized by the characteristic temperature derived from H- and He-like line flux ratios) tend to show densities derived from O VII of no more than a few times 10^{10} cm^{-3}, whereas no definitive trend is found for the more active stars. Investigating the densities of the hotter plasma with various Fe XXI line ratios, we found that none of the spectra consistently indicates the presence of very high densities. We argue that our measurements are compatible with the low-density limit for the respective ratios ($\approx 5 \times 10^{12}$ cm^{-3}). These upper limits are in line with constant pressure in the emitting active regions.
We focus on the commonly used Rosner et al. (1978) scaling law to derive loop lengths from temperatures and densities assuming loop-like structures as identical building blocks. We derive the emitting volumes from direct measurements of ion-specific emission measures and densities. Available volumes are calculated from the loop-lengths and stellar radii, and are compared with the emitting volumes to infer filling factors. For all stages of activity we find similar filling factors up to 0.1.

Key words. X-rays: stars – stars: coronae – stars: late-type – stars: activity – techniques: spectroscopic

1. Introduction

The magnetic outer atmosphere of the Sun, the corona, was recognized in radio and X-ray emission. While the radio emission is associated with bremsstrahlung and cyclotron emission from free electrons in the hot plasma, the X-ray emission is produced by bremsstrahlung and line emission. Stellar coronal activity is therefore investigated primarily in these two bands of the electromagnetic spectrum. We focus on the potentials offered by X-ray spectroscopy of stellar coronae. Systematic measurements with Einstein, ROSAT, ASCA, and other satellite-based X-ray missions revealed that all late-type main sequence stars from type M to F have coronal X-ray emission. Schmitt (1997) found X-ray surface fluxes covering four orders of magnitude. Coronal activity appears thus to be a universal process for cool stars of spectral types F-M, but no correlation between spectral type and degree of activity could be established. The only fundamental stellar parameter found to be correlated with the X-ray luminosity is the rotational velocity $v \sin i$ (and thus age, e.g., Pallavicini et al. 1981), suggesting that a magnetic dynamo process is involved in producing the X-ray coronae. Some information on the spatial distribution of coronal plasma was inferred by indirect means such as modeling of eclipses and rotational modulation (e.g., White et al. 1990; Schmitt & Kürster 1993; Güdel et al. 1995, 2003; Siarkowski et al. 1996), but such analyses can only be carried out for very special systems with advantageous geometries. X-ray spectra allow us to gather a more general insight into the physical properties of a large variety of stellar coronae. The analysis of X-ray coronae has in the past been possible only with very limited spectral resolution or with low sensitivity. Plasma densities (as the subject of this work) could not be measured from these spectra, because information from spectral lines was not available. Nevertheless, temperature distributions (or emission measure distributions EMD) and coronal abundances could be estimated

⋆ Appendix A is only available in electronic form at
http://www.edpsciences.org

from low-resolution spectra by the application of global fit approaches. A model spectrum composed of a continuum and all known emission line fluxes formed under assumed temperature conditions and with assumed elemental abundances (mostly only scaled to solar abundances) is iterated using one or two temperature components left free to vary. The information on bremsstrahlung continuum and emission lines is extracted from atomic databases containing line emissivities as a function of plasma temperature under assumptions of solar elemental composition and collisionally ionized plasma. A spectral model is thus composed as the sum of bremsstrahlung and all lines formed under the assumption of thermal equilibrium, and model parameters are the equilibrium temperature and elemental abundances. The first detailed survey of low resolution X-ray spectra for a large sample of 130 late-type stars ($B-V$ colors redder than 0.0) was presented by Schmitt et al. (1990) using Einstein data. For each spectrum the temperature structure was obtained with global spectral models. Different approaches were tested ranging from isothermal plasma with one or two (absorbed) temperature components to continuous emission measure distributions. A much smaller sample concentrating on a sample covering the Sun in time was analyzed by Güdel et al. (1997) using ROSAT and ASCA data. Their sample consisted of nine G stars in different stages of evolution. From MEKAL and Raymond-Smith models they found that the older stars (with slow rotation) contained only a single cool temperature component in the emission measure distribution while the younger, more active stars had a bimodal emission measure distribution with a similar cool component and an additional hot component apparently independent of the cooler component suggesting an additional heating mechanism for the more active stars. The hotter temperature component $T_{\rm hot}$ was found to scale with the X-ray luminosity $L_{\rm X}$:

$$L_{\rm X} \approx 55\, T_{\rm hot}^4 \ \text{(in cgs units)}. \quad (1)$$

The other crucial parameter that determines heating, cooling, and geometric properties of a stellar corona is the electron density. It is responsible for the time scale of physical changes (e.g., via the sound and Alfvén velocity), and, together with the temperature, controls the emissivity of a plasma. Since the densities $n_{\rm e}$ are the missing parameter linking emitting volumes V and emission measures $EM = n_{\rm e}^2 V$, these measurements are very important for calculating the sizes of X-ray emitting regions. Scaling laws derived from the solar corona relate spatial structure to temperatures and densities. Independently determined densities and temperatures thus make it possible to access semi-loop lengths. The two structural parameters loop length and emitting volume can only be obtained with measurements of emission measures, temperatures, and densities. In contrast to rare and often extreme stellar systems like eclipsing binaries, density measurements open up a new avenue to coronal structure recognition since we can apply them to all stars of sufficient brightness.

Despite relatively good spatial resolution with previous X-ray satellites, the technology of their photon counting detectors reached only moderate spectral resolution in the X-ray regime. Very few attempts were made to use dispersive gratings converting spatial resolution into spectral resolution with the potential to resolve individual emission lines. For grating spectroscopy sufficient light is needed and it is therefore only feasible for the brightest sources with long exposure times. In the extreme ultraviolet range this technique has been successfully applied, e.g., with the EUVE mission. Many low-temperature Fe lines from stages Fe X to Fe XVI can be measured with EUVE and are sensitive to densities (Schmitt et al. 1994). Also, at higher temperatures density-sensitive Fe lines can be measured with EUVE (Dupree et al. 1993), but they are only sensitive for relatively high ranges of density $n_{\rm e} > 10^{11}\,{\rm cm}^{-3}$. A summary of results from EUVE measurements is presented by Bowyer et al. (2000). Since the density information is inferred from mostly weak lines the results tend to be ambiguous. The hotter plasma regions of Capella and AB Dor were investigated by Dupree et al. (1993); Sanz-Forcada et al. (2003a) using Fe XIX-XXII line ratios. Densities as high as $10^{13}\,{\rm cm}^{-3}$ were reported, suggesting very compact emission regions. However, later Chandra LETGS measurements of Capella contradict these results (Mewe et al. 2001). Because of low sensitivity, EUVE data could only be obtained for some bright sources such as Capella or AB Dor. The apertures of the new missions Chandra and XMM-Newton are large enough to allow grating spectroscopy for many stellar coronae, and X-ray spectra of unprecedented spectral resolution are available. We are able now to measure densities and temperatures from line flux ratios. In this paper we describe the formalism for calculating densities from selected emission line fluxes in Sect. 2. We then present the results from density-sensitive ratios representative for O VII and Ne IX plasma as well as carbon-like Fe XXI lines in Sect. 4. In Sect. 6 we discuss our results.

2. Analysis

2.1. Density measurement

Spectroscopic information on coronal plasma densities for stars other than the Sun first became possible with the advent of high resolution EUVE spectra ($\lambda/\Delta\lambda \sim 200$; Abbott et al. 1996) that allowed the separation of individual spectral lines. Even with this resolution the available diagnostics often tended to be ambiguous because of the poor signal-to-noise ratio of observed spectra or due to blended lines. Studies of density-sensitive lines of Fe XIX to Fe XXII in EUVE spectra of the RS CVn system Capella revealed some evidence for high densities of $n_{\rm e} \sim 10^{12}$ to $10^{13}\,{\rm cm}^{-3}$ at coronal temperatures near 10^7 K reported by Dupree et al. (1993), but often the densities derived from different lines or ions varied greatly despite the similar formation temperatures. More recent analyses of EUVE Fe XIX-XXII lines (Sanz-Forcada et al. 2003a) and Chandra HETGS Fe XXI lines for AB Dor (Sanz-Forcada et al. 2003b) also returned high densities $\log n_{\rm e} > 12.3$, but again, not consistently for all considered lines. Since many of the lines used in the analyses are intrinsically faint, even the HETGS data suffer from rather low signal-to-noise. Also the consequences of unidentified blends can be more severe for faint lines, which could be the reason for the discrepant densities derived from Fe lines in the same ionization stage.

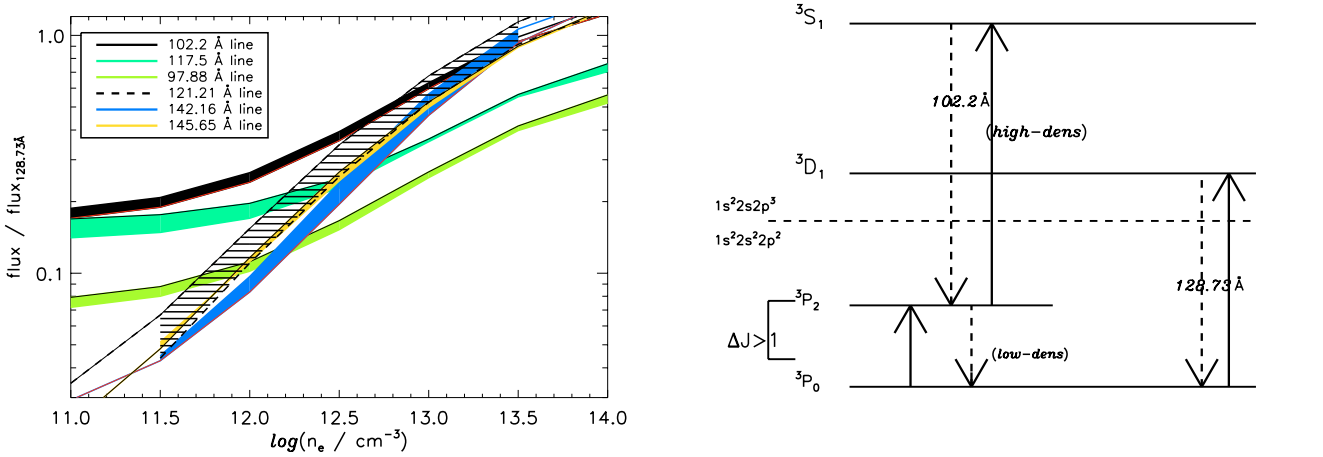

Fig. 1. Density-sensitive Fe XXI line flux ratios as predicted by the APEC database for the temperature range between $\log(T) = 6.6$ (*lower borders*) and 7.6 (*upper borders*). In the right panel we show the term diagram explaining the formation of the 102.22 Å line as an example.

The spectrometers on board the X-ray telescopes Chandra and XMM-Newton make it possible to measure emission lines at wavelengths shorter than 95 Å with far better signal to noise and spectral resolution. In particular, the Fe L-shell and M-shell lines and lines of the He-like ions from carbon to silicon are available for density measurements. A few of the density-sensitive Fe lines measurable with EUVE in the 120 Å range can also be measured with the Low Energy Transmission Grating Spectrometer (LETGS) on board *Chandra* but only upper limits were found by Mewe et al. (2001) ($n_e < 2{-}5 \times 10^{12}$ cm^{-3}). They point out that the Fe XIX to Fe XXII line ratios are only sensitive above $\sim 10^{11}$ cm^{-3}, so that no tracer for low densities for the hotter plasma component is available, neither with EUVE nor with *Chandra* or XMM-Newton.

2.2. Theoretical background

The XMM-Newton and *Chandra* grating spectra allow high precision measurements of individual line fluxes and line flux ratios. Line fluxes are used to compute emission measures in specific lines, which can be combined to differential emission measure distributions (e.g., Ness et al. 2003a; Schmitt & Ness 2004). Ratios of certain line fluxes are sensitive to temperatures or densities and can be used to describe local conditions in stellar coronae describing the physical conditions in the line-forming regions. In this paper we analyse the He-like triplets of oxygen and neon that probe the low-temperature component of the plasma, and four density-sensitive Fe XXI lines that probe the hotter component of the plasma in a larger sample of stars.

2.2.1. Density diagnostics with carbon-like ions

With six electrons ($1s^2 2s^2 2p^2$) the Fe XXI ion is carbon-like. Its ground configuration is split into the states $^3P_0$ (ground state), $^3P_1$, $^3P_2$, $^1D_2$, and $^1S_0$. Transitions within the ground configuration, which are naturally forbidden by definition, do occur; for example, the $^3P_1$–$^3P_0$ transition is located at 1354 Å observable with HST (e.g., Robinson et al. 1994; Linsky et al. 1998). Fe XXI at UV and X-ray wavelengths involve transitions from the $^3S_1$ and $^3D_1$ states of the excited configuration $1s^2 2s 2p^3$ (see term diagram in right panel of Fig. 1).

Collisional excitations from the ground state $^3P_0$ predominantly occur into the excited $^3D_1$ state, producing the strong extreme ultraviolet (XUV) Fe XXI at 128.73 Å, which is essentially independent of density and can be used as a reference line reflecting the Fe abundance and the ionization balance for the stage Fe XXI. Collisional excitation from the ground state into the $^3S_1$ state of the excited configuration is much less likely than collisional excitation from the "excited" ground state $^3P_2$–$^3S_1$. The population of the state $^3S_1$ of the excited configuration therefore depends critically on the population of the state $^3P_2$. In a low-density plasma the population of the latter will be small and eventually decay radiatively into the $^3P_0$ level; in a high density plasma the $^3P_2$ state will be collisionally depopulated into the $^3S_1$ level of the excited configuration, which in turn decays radiatively into $^3S_1$–$^3P_2$ (102.22 Å) or $^3S_1$–$^3P_1$ (97.88 Å). The latter two transitions are therefore density-sensitive, because they depend on the density-sensitive population of the $^3P_2$ state. Similar considerations apply to the ground- and excited levels $^3P_1$ and $^3P_2$ (Mason et al. 1979) leading to transitions at $^3P_1$–$^3P_1$ (117.5 Å), and $^3P_2$–$^3P_2$ (121.21 Å). All these lines are in the band pass of the *Chandra* LETGS and can be used to estimate densities of the Fe XXI emitting plasma at $T \sim 10$ MK. In Fig. 1 we show predicted line flux ratios as a function of density (theoretical emissivities were taken from the APEC database, e.g., Smith et al. 2001)[1]. Although these lines are all in the same ionization stage, the line flux ratios depend slightly on the plasma temperature. This is illustrated by the associated curves for a low temperature $\log(T) = 6.6$ and a high temperature $\log(T) = 7.6$ for each ratio in Fig. 1. Clearly, temperature primarily affects the low-density limit. To be conservative we will use the high-temperature

[1] Version 1.2; available at `http://cxc.harvard.edu/atomdb`

theoretical ratios for comparison with our measured ratios, yielding higher theoretical line flux ratios.

2.2.2. Density diagnostics with helium-like ions

The derivation of densities with He-like triplets originated in solar observations (Gabriel & Jordan 1969). The excited state transitions $^1P_1$, $^3P_1$, and $^3S_1$ to the ground state $^1S_0$ are by convention named resonance line (r), intercombination line (i), and forbidden line (f), respectively. The ratio f/i is density-sensitive due to collisional excitations $^3S_1 \rightarrow {}^3P_1$ in high-density plasmas. These transitions compete with radiative transitions induced by possible external radiation sources, namely the stellar surface. An analytical description was given by, e.g., Gabriel & Jordan (1969); Blumenthal et al. (1972):

$$\frac{f}{i} = \frac{R_0}{1 + n_e/N_c + \phi/\phi_c} \quad (2)$$

with R_0 being the low density limit (an atomic parameter derived from a weighted ratio of Einstein A-coefficients), N_c the critical density where f/i drops to half the low-density limit R_0, and ϕ/ϕ_c describing the influence from external radiation fields. The values for these coefficients depend on the atomic number Z and slightly on plasma temperature. For our analysis we use the ions from $Z = 8$ (i.e., O VII) and $Z = 10$ (Ne IX). The parameters in Eq. (2) are taken from Pradhan & Shull (1981) with $R_0 = 3.95$ and $N_c = 3.1\times10^{10}$ cm^{-3} for O VII and $R_0 = 3.4$ and $N_c = 5.9\times10^{11}$ cm^{-3} for Ne IX. The parameter ϕ/ϕ_c is commonly neglected, since most active stars have no critical levels of photospheric UV emission; nevertheless we will derive this parameter for the hottest photospheres in our sample according to Ness et al. (2002a). The functional dependence of the f/i ratio according to Eq. (2) with varying electron density is illustrated in Fig. 2 in comparison with predictions from the CHIANTI database version 4.0 with ionization balances from Arnaud & Rothenflug (1985) (Dere et al. 2001; Young et al. 2003), the APEC database, and Porquet et al. (2001) for the temperature range 1–4 MK for O VII and 4–9 MK for Ne IX. It can be seen that within the given temperature range the analytical determination of densities according to Eq. (2) is consistent with the other predictions.

2.2.3. Previous work

Since the gratings were to a large extent designed to measure the He-like triplets of N VI up to Si XIII it is not surprising that such analyses have been carried out for quite a few individual sources (e.g., Audard et al. 2001; Güdel et al. 2001; Ness et al. 2001, 2002c, 2003a; Stelzer & Schmitt 2004). Especially the O VII triplet has been analyzed, because the lines are strongest and least blended. From the measured f/i-ratios densities were calculated. For Capella and Procyon the densities were found to be at the lower end of the sensitivity range (Ness et al. 2001). The first study of f/i-ratios in a sample of stellar coronae was carried out by Ness et al. (2002d), who measured *f/i*-ratios for all He-like ions measurable with the LETGS for a sample of ten stellar coronae. For inactive stars (with low $L_X \sim 10^{27}$ erg/s) only low density limits were found, while

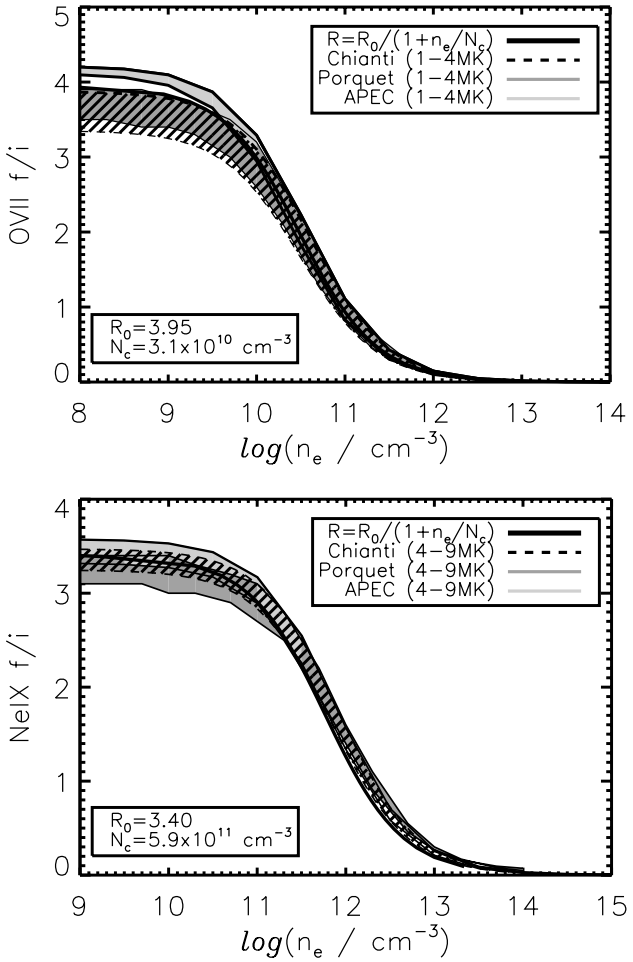

Fig. 2. Comparison of theoretical predictions for density sensitive *f/i* ratios for O VII (*top panel*) and Ne IX (*bottom panel*) from Eq. (2), the CHIANTI database, Porquet et al. (2001), and the APEC database. Filled areas represent the varying electron temperatures as given in the legends (hatched: CHIANTI, dark-grey shaded: Porquet et al. (2001), light-shaded: APEC). Lower temperatures yield lower *f/i* ratios.

for the active stars in their sample higher densities were encountered, although a little surprisingly only low-density limits were measured for some RS CVn stars. Ness et al. (2002d) concluded that for the high-temperature plasma LETGS data offer no conclusive tracer for densities because of blending problems with the Ne IX triplet, which is better measured with the HETGS (see also Ness et al. 2003a). Especially for the more active stars only a very small fraction of the X-ray emitting plasma is produced in the temperature range where the O VII triplet is produced.

The purpose of this paper is the analysis of He-like f/i ratios for a large sample of X-ray spectra obtained with the Reflection Grating Spectrometer (RGS) on board XMM-Newton and the Low Energy Transmission Grating (LETGS) and the High Energy Transmission Grating Spectrometers (HETGS; consisting of the Medium Energy Grating MEG and the High Energy Grating HEG) on board *Chandra*. The LETGS spectra are also used to measure density-sensitive Fe XXI lines. The aspect of resonant line scattering in stellar coronae has been addressed with a large sample of grating spectra

(Ness et al. 2003b) and strong evidence is found that opacity effects can generally be neglected in coronal plasmas. We apply the same procedures for data reduction as in Ness et al. (2003b). For internal consistency, the LETGS spectra presented by Ness et al. (2002d) are re-analyzed and included in our sample. We focus on density measurements with the O VII and Ne IX triplets and Fe XXI ratios, and estimate systematic emitting volumes and filling factors for the different coronae.

2.3. Measurement of line fluxes

We prefer to measure line counts with a program developed specifically for this task named named CORA (Ness & Wichmann 2002). The *lheasoft* package XSPEC can also do the job, but for a large number of different spectra the CORA program is more efficient.

2.3.1. Systematic errors from line profile modeling

The CORA program measures line counts from the raw spectrum, i.e., the instrumental background is not subtracted and the background spectrum is instead added to the iterated model spectrum. While the measurement of line counts for the Chandra gratings is straightforward (Ness et al. 2003b), more difficulties arise for RGS spectra. For Capella and AB Dor we measured RGS line counts with both CORA and XSPEC (convolving a δ-function profile with the line spread function) and we found consistent results within the 1σ errors. However, line fluxes obtained with the CORA program were found to be systematically lower than the results obtained with XSPEC. A possible reason for these systematic discrepancies could be that XSPEC uses a wavelength-dependent response matrix, which provides a more accurate instrument description than CORA (which uses only approximate analytical line profiles). We tested the effects arising from different treatments of the instrumental line profiles by exporting the line profiles used for the XSPEC fits into CORA and found similar results compared to what we obtained using the analytical Lorentzian profile function, without any systematic trend. Obviously the Lorentzian used by CORA is an adequate representation for the RGS line profiles for our purposes.

2.3.2. Systematic errors from background modeling

Another source of systematic errors is the estimation of source background. As source background we consider the combination of continuum emission and the sum of unresolved weak lines above the measured instrumental background. This problem has been extensively described by Ness et al. (2003b) who developed a modified median routine providing a parameterized method to determine a source continuum value. We present an alternative approach, viz. a χ^2 optimization of the source continuum.

In the CORA program the continuum is assumed to be constant in sufficiently small wavelength regions, which is justified for individual line fitting with nearby lines. However, use of the median value as a source background value as applied in the CORA program is only valid as long as more than 50% of the bins belong to the desired background. A significant difference between the LETGS, for which the CORA program was originally developed, and the RGS spectra in our sample is the profile function. The wings of the RGS line profile are wider and contribute to the continuum value obtained with the median function and CORA will therefore return an overestimated continuum and thus underestimated line counts. Our modified method uses the median value as a start value and we minimize the χ^2 value iterating only the source background value. The other parameters of the model spectrum (wavelengths and line widths) are kept fixed to the given initial values but the line counts are optimized with the implemented likelihood method in each iteration step.

We tested the new procedure and found it stable and particularly useful for wavelength regions with few emission lines. For RGS spectra this method returned systematically lower source background values, while for LETGS spectra these values were consistent with the median values. The discrepancies with the XSPEC results are significantly reduced. We point out that even without the new procedure the discrepancies are not significant within the errors. We also tested the χ^2 fit procedure for the Fe XVII lines measured by Ness et al. (2003b), but found that it did not work well. We attribute these difficulties to the large number of lines in the 15 Å region. The disadvantage of our χ^2 approach is that all line features not selected to be measured as emission lines increase the source background value in the attempt to minimize the χ^2 value in those wavelength regions. We thus conclude that the parameterized median value must be used for line-crowded regions, while the χ^2 approach represents a non-parameterized procedure for measuring in wavelength regions where all line features are selected to be fitted.

3. Observations

For our study of stellar coronae we selected a sample of coronal sources as large as possible. We gathered 64 grating spectra of 42 stellar coronae; we specifically discuss 22 RGS spectra, 16 LETGS spectra, and 26 HETGS spectra. The reduction of the spectra has been carried out with standard SAS and CIAO routines and is described by Ness et al. (2003b). The details of the observations with exposure times and derived luminosities are summarized in Table 1 of Ness et al. (2003b). X-ray luminosities, averaged over the complete observations (i.e., including flares), are obtained by summing up all dispersed photons in the wavelength range 5.15–38.19 Å after consideration of $A_{\rm eff}(\lambda)$. In order to have the largest possible data sample for our systematic analysis of densities we extracted all additional stellar spectra that were publicly available by 31 January 2004 from the Chandra archive. These additional observations are listed in Table 1 using the same format as in Ness et al. (2003b). For internal consistency the LETGS observations of Algol and Capella were reanalyzed for this work and the results are also listed in Table 1 for comparison. We extracted effective areas for flux conversion from the Capella observations and used these areas for all observations. Since this paper deals only with line ratios (and therefore uses only ratios of effective areas),

Table 1. Properties of observations not already described in Ness et al. (2003b).

Star	Exposure time [ks]			$L_X(10^{28}$ erg/s)						
	RGS1,2	LETG	HEG/	RGS1[a]		RGS2[a]		LETG[a]	MEG[a]	HEG[b]
			MEG	1st order	2nd order	1st order	2nd order			
AD Leo	36.25	48.50	45.16	3.50	3.01	3.07	2.03	3.93	3.19	1.88
λ And	31.83	98.59	81.91	249.61	238.61	295.03	188.31	935.90	198.33	121.17
σ^2 CrB	19.31	–	83.72	322.59	338.72	307.83	312.74	–	305.60	154.81
Capella	52.92	226.42	154.68	145.38	157.22	168.06	132.10	186.56	153.08	127.43
Algol	52.66	79.53	51.73	283.73	–	–	–	944.99	673.63	557.72
II Peg	–	–	42.74	–	–	–	–	–	1318.60	1045.50
44 Boo	–	–	59.14	–	–	–	–	–	45.35	41.36
Prox Cen	–	–	42.39	–	–	–	–	–	0.03	0.03
ER Vul	–	–	112.01	–	–	–	–	–	240.10	258.20
TY Pyx	–	–	49.13	–	–	–	–	–	532.60	550.70
24 UMa	–	–	88.90	–	–	–	–	–	125.04	86.16
ξ UMa	–	–	70.93	–	–	–	–	–	14.87	16.45
V824 Ara	–	–	94.23	–	–	–	–	–	254.66	212.00
31 Com	–	–	130.19	–	–	–	–	–	6461.70	12301.80
HD 223460	–	–	95.66	–	–	–	–	–	3289.00	3551.00
Canopus	–	–	94.55	–	–	–	–	–	322.00	316.10
μ Vel	–	–	134.06	–	–	–	–	–	123.40	146.45
IM Peg	–	–	95.03	–	–	–	–	–	2520.70	2316.90
Speedy Mic	–	–	69.00	–	–	–	–	–	223.00	100.40
V471 Tau	–	87.49	–	–	–	–	–	112.34	–	–
VW Cep	–	101.17	–	–	–	–	–	70.42	–	–

[a]5.15–38.19 Å. [b]5.15–21.5 Å.

this procedure is sufficiently accurate. Nevertheless we compared these effective areas with individually extracted areas and found sufficient agreement for all instruments. The complete stellar sample used for this work is described in Sect. 3.2 and all stellar properties relevant for this paper are listed in Table 2.

3.1. Measured line counts

For this paper we measure the O VII triplet (21.6/21.8/22.1 Å, $\log(T_m/K) = 6.3$) and the Ly$_\alpha$ line of O VIII (18.97 Å, $\log(T_m/K) = 6.5$) with the RGS1, the LETGS, and the MEG. The RGS2 cannot measure O VII because of chip failure, and the HEG does not cover the O VII triplet. The Ne IX triplet (13.44/13.55/13.7 Å, $\log(T_m/K) = 6.6$) is severely blended with highly ionized Fe lines (Ness et al. 2003a) and the blends can only be resolved with the HEG and the MEG. Although the RGS and LETGS cover the 13.5 Å region we do not analyze those data here, because de-blending is too complicated and must be done in a future paper. The measured counts and derived *f/i* ratios (using effective areas as described in Ness et al. 2003b) are listed in Tables A.2 and A.5. The densities derived from Eq. (2) are also listed with additional description in Sect. 4.2.2. For the hot sources for which LETGS spectra are available, we measured the lines at 128.73 Å, 117.5 Å, 102.22 Å, and 97.87 Å. The measured line counts are listed in Table 3 and discussed in Sect. 4.2.1.

3.2. Description of the stellar sample

In Table 2 we list all relevant stellar parameters. The spectral type information has been taken from the Simbad database[2]. It can be seen that a broad range of coronae is included in the sample. The sample covers stars with extremely high flare activity, RS CVn systems, and other double systems. The distances are also from Simbad and are based on Hipparcos parallaxes. An important parameter for our analysis is the stellar radius which is needed for scaling the derived coronal loop sizes to typical geometries. For some stars in the sample radii are not available in the literature, and we adopted a procedure to calculate stellar radii from the apparent visual magnitudes V and distances (and thus absolute magnitudes) and spectral types, listed in Table 2. We estimate bolometric corrections and effective temperatures $T_{\rm eff}$ from the spectral type interpolating tables from Kaler (1989). We use the bolometric luminosity $L_{\rm bol}$, calculated from the absolute luminosity and the bolometric correction to calculate the stellar radius for each star from $L_{\rm bol} = 4\pi R_\star^2 \sigma T_{\rm eff}^4$ with σ the Stefan-Boltzmann constant. In Table 2 we list the effective temperatures thus derived, bolometric luminosities, and stellar radii in comparison to what we found in the literature. Good agreement with most values from the literature is found and we use our derived radii for further analysis. In the last column we list the X-ray

[2] http://simbad.u-strasbg.fr/

Table 2. Description of the stellar sample.

Star	HD/Gl	Spectr. Type[a]	Distance[a]	V^a	B.C.[b]	$T^b_{\rm eff}$	$\log(L_{\rm bol})$	$R^c_\star$	$R^d_\star$	$L^e_{\rm X}$
			pc	mag	mag	K	erg/s	$[R_\odot]$	$[R_\odot]$	10^{28} erg/s
24 UMa	82210	G4.0III-IV	32.37	4.57	–0.07	5666	34.72	3.2	3.82	218.00
31 Com	111812	K2.0	335.60	9.26	–2.17	4780	34.94	6.38	6.89	0.00
44 Boo	133640	G2.0V/G2.0V	12.76	4.76	–2.46	5780	33.83	0.87/0.6	1.31	49.60
47 Cas	12230	G2.0V/F0.0Vn	33.56	5.27	–0.19	5780	34.46	1.0	2.73	236.07
AB Dor	36705	K1.0IIIp	14.94	6.93	–0.06	5010	33.15	1.0	0.81	150.00
α Cen A	128620	G2.0V	1.34	0.01	–0.06	5780	33.77	1.23	1.23	0.13
α Cen B	128621	K0.0V	1.34	1.34	–0.10	5240	33.28	0.8	0.85	0.20
AD Leo	Gl388	M3.5V	4.70	9.43	–0.15	3295	31.93	0.5	0.45	7.22
Algol	19356	B8.0V/K2.0III	28.00	2.12	–0.04	13400	35.88	3.5	2.59	661.00
AR Lac	210334	G2.0IV/K0.0IV	42.03	6.13	–0.19	5780	34.31	1.54/2.8	2.30	1050.00
AT Mic	196982	dM4.5/M4.5	10.22	10.25	–0.22	3175	32.39	–	0.84	29.40
AU Mic	197481	M0.0	9.94	8.61	–0.07	3920	32.52	0.67	0.63	55.49
β Cet	4128	K0.0III	29.38	2.04	–1.20	5240	35.69	11.6	13.58	268.52
Canopus	45348	F0.0II	95.88	–0.72	–0.06	7240	37.77	–	78.66	0.00
Capella	34029	G1.0III/K0.0I	12.94	0.08	–2.17	5850	35.71	9.2/13	11.17	419.16
χ^1 Ori	39587	G0.0V	8.66	4.41	–2.17	5920	33.63	1.1	0.99	12.00
EK Dra	129333	dG0.0e	33.94	7.61	–0.10	5920	33.53	–	0.89	102.07
ϵ Eri	22049	K2.0V	3.22	3.73	–0.07	4780	33.11	0.81	0.84	2.10
EQ Peg	Gl896	M3.5/M4.5	6.25	10.32	–0.10	3295	31.82	0.4/0.26	0.40	3.97
ER Vul	200391	G0.0V/G5V	49.85	7.36	–2.46	5920	33.97	1.07	1.47	376.00
EV Lac	Gl873	M3.5	5.05	10.09	–0.85	3295	31.73	0.34	0.36	12.25
HD 223460	223460	G1.0III	134.95	5.90	–0.04	5850	35.42	–	7.99	1691.10
HR 1099	22468	G5.0IV/K1.0IV	28.97	5.91	–0.25	5610	34.09	3.9/1.3	1.89	1512.10
II Peg	224085	K0.0V	42.34	7.37	–1.34	5240	33.87	4.5	1.68	650.00
IM Peg	216489	K1.5II-IIIe	96.80	5.90	–0.07	4895	35.20	26.2	8.85	2756.10
κ Cet	20630	G5.0Vvar	9.16	4.83	–0.19	5610	33.52	0.94	0.98	7.72
λ And	222107	G8.0III	25.81	3.82	–0.19	5490	34.85	7.5	4.70	335.00
μ Vel	93497	G5.0III/	35.50	2.72	–0.07	5610	35.54	10.	10.04	0.00
π^1 UMa	72905	G1.5Vb	14.27	5.64	–2.88	5815	33.57	1.0	0.96	12.83
Procyon	61421	F5.0IV-V	3.50	0.34	–0.06	6540	34.46	2.06	2.12	1.90
Prox Cen	Gl551C	M5.5Ve	1.29	11.05	–0.10	3043	30.44	0.15	0.10	0.17
σ^2 CrB	146361J	F6.0V/G0.0V	21.70	5.64	–0.09	6450	33.92	1.1	1.18	460.61
Speedy Mic	197890	K0.0V	44.40	9.44	–0.06	5240	33.08	0.73	0.68	0.00
TY Pyx	77137	G5.0IV/G5.0IV	55.83	6.90	–0.22	5610	34.27	1.59/1.6	2.31	463.00
UX Ari	21242	G5.0V/K0.0IV	50.23	6.47	–0.25	5610	34.34	4.7/0.93	2.53	1205.00
V471 Tau	17962	K0.0	46.79	9.48	–0.06	5240	33.11	0.85	0.70	185.10
V824 Ara	155555	K1.0Vp	31.42	6.88	–0.08	5010	33.82	–	1.74	449.30
VW Cep	197433	K0.0Vvar	27.65	7.38	–0.10	5240	33.50	0.88	1.09	105.00
VY Ari	17433	K0.0	43.99	6.76	–0.23	5240	34.15	1.9	2.31	1243.63
ξ UMa	98239	G0.0V	8.80	3.78	–0.19	5920	33.89	0.94	1.35	30.50
YY Gem	60179C	M0.5V/M0.5V	15.80	9.07	–0.19	3800	32.80	0.66	0.93	82.37
YZ CMi	Gl285	M4.5V:e	5.93	11.12	–0.19	3175	31.57	0.36	0.33	4.44

[a]From Simbad. [b]From Kaler (1989). [c]Literature.
[d]From $L_{\rm bol} = 4\pi R^2_\star \sigma T^4_{\rm eff}$ (used for analysis). [e]Measured with ROSAT (5.2–124 Å).

luminosity from ROSAT (e.g., Hünsch et al. 1999, wavelength range 5.2−124 Å). In Fig. 3 we compare these values with X-ray luminosities obtained from the new spectra (wavelength range 5.15−38.2 Å) listed in Tables A.1 and A.4. The regression fit has a slope slightly lower than one, indicating that the ROSAT fluxes for the more active stars have been

Table 3. Measured Fe XXI counts obtained from the available LETGS spectra.

	128.73 Å	117.5 Å	102.22 Å	98.87 Å
transm.[a]	0.8050	0.8491	0.8993	0.9115
$A_{\rm eff}/{\rm cm}^2$	3.67	6.17	6.71	7.24
β Cet	587.4 ± 31.6	178.8 ± 23.1	198.9 ± 24.7	98.20 ± 17.6
λ And	471.4 ± 29.4	139.5 ± 20.7	144.3 ± 24.9	109.7 ± 18.9
AD Leo	61.17 ± 14.2	15.48 ± 11.7	21.64 ± 12.9	14.89 ± 9.14
Algol	354.0 ± 25.4	120.3 ± 19.4	145.3 ± 19.9	77.86 ± 14.3
Capella	1086. ± 43.1	501.7 ± 33.9	362.0 ± 36.6	69.97 ± 21.1
EK Dra	52.02 ± 10.4	28.27 ± 11.5	9.360 ± 12.1	–
HR1099	386.8 ± 25.6	156.4 ± 19.6	142.3 ± 22.2	63.43 ± 15.4
UX Ari	167.6 ± 19.3	71.58 ± 17.6	35.31 ± 17.0	55.07 ± 13.0
YY Gem	46.10 ± 10.5	29.74 ± 10.7	8.531 ± 9.01	17.86 ± 7.87

[a]ISM transmission using N(HI) = 10^{18}, N(HeII)/N(HI) = 0.09, N(HeII)/N(HI) = 0.01.

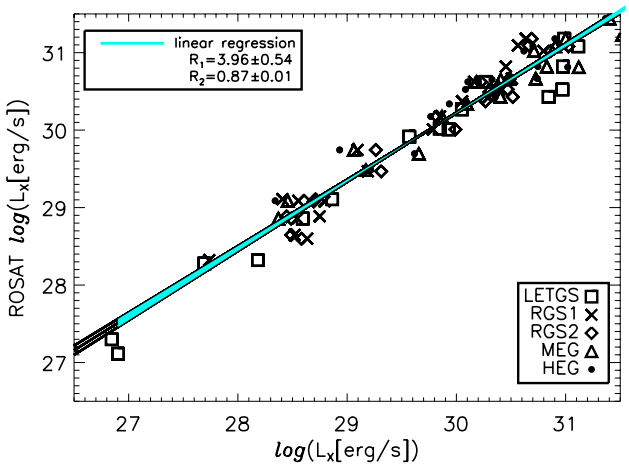

Fig. 3. Comparison of ROSAT luminosities (5.2−124 Å) listed in Table 2 with $L_{\rm X}$ measurements for RGS1, RGS2, LETGS, MEG (5.15−38.2 Å), and HEG (5.15−21.5 Å) from Ness et al. (2003b) and Table 1. The regression curve $\log L_{\rm X}({\rm ROSAT}) = R_1 + R_2 \log L_{\rm X}({\rm Chandra/XMM})$ with parameters R_1 and R_2 as given in the legend is overplotted. The slope R_2 is near unity, indicating good cross-calibration between instruments.

underestimated. With the best-fit regression parameters the discrepancies are no higher than a factor of two.

4. Results

4.1. Temperatures from H-like and He-like line ratios

In the past, coronal temperatures were estimated via global spectral fits from low-resolution spectra. With high-resolution spectra now available we can additionally determine average coronal temperatures by considering individual line fluxes, that yield a temperature characterizing the formation of, e.g., the O VII triplet. The ratios of line fluxes originating from adjacent ionization stages of the same chemical element allow the determination of temperatures independent of the respective elemental abundances. Since for the conversion of measured line fluxes to plasma temperatures and for the construction of synthetic spectra from global plasma emission models the same databases are used, the systematic errors are basically the same. However, a careful choice of strong lines for the calculation of line ratios can reduce systematic errors, since strong lines are mostly not as much affected by uncertainties as weaker lines. Also, line blends from unidentified weaker lines cannot harm strong lines as much as weaker lines. A detailed discussion of the interpretation of line ratios and global fit approaches is given in Güdel (2004).

The strongest lines in the grating spectra are the H-like and He-like lines of carbon, nitrogen, oxygen, neon, magnesium, and silicon. We measured the line fluxes of these lines in order to calculate temperature-sensitive ratios for these ions for each star in our sample. In Fig. 4 we show our results plotted vs. the total X-ray luminosities (cf. Tables A.1 and A.4 for oxygen); a clear trend can be recognized for all ions. We overplotted best-fit linear regressions and find decreasing slopes for increasing Z, thus increasing formation temperatures of the H-like and He-like states. A correlation of plasma temperature with the degree of activity has long been known (e.g., Schrijver et al. 1984; Schmitt et al. 1990). In terms of a putative emission measure distribution, this trend would indicate a predominance of higher emission measure at higher temperature in stars with a higher activity level. When considering H- and He-like lines of individual elements, this trend should be reflected in a larger ratio of H-like to He-like line fluxes in the more active stars, and this is what we now recover from our analysis.

A continuous temperature distribution suggests a mixture of temperatures making the adjacent lines an ideal means for defining interpolation points fixing the shape of the temperature distribution. Such an approach has been introduced by, e.g., Schmitt & Ness (2004) for finding abundance-independent emission measure distributions. For our purposes we can conclude that the temperatures derived from the line ratios of H-like and He-like lines characterize the plasma conditions around the plasma that produces the He-like lines used for the density analysis.

4.2. Densities from line flux ratios

We measured line fluxes from both density-sensitive He-like lines and carbon-like Fe XXI lines. With the He-like lines we probe only the "cool" plasma component, while with the Fe XXI densities we probe the "hotter" coronal components.

4.2.1. Densities from Fe XXI line flux ratios

As described in Sect. 2.2.1 the Fe XXI density diagnostics are essentially based on the appearance of certain lines in high-density plasmas. Our search for densities exceeding $\log n_{\rm e} = 11$ is therefore based on detections of these density-sensitive lines. In Table 3 we list the results for our Fe XXI line count measurements. Table 3 reveals that for all stars studied the reference line at 128.73 Å is the strongest line, yielding flux ratios

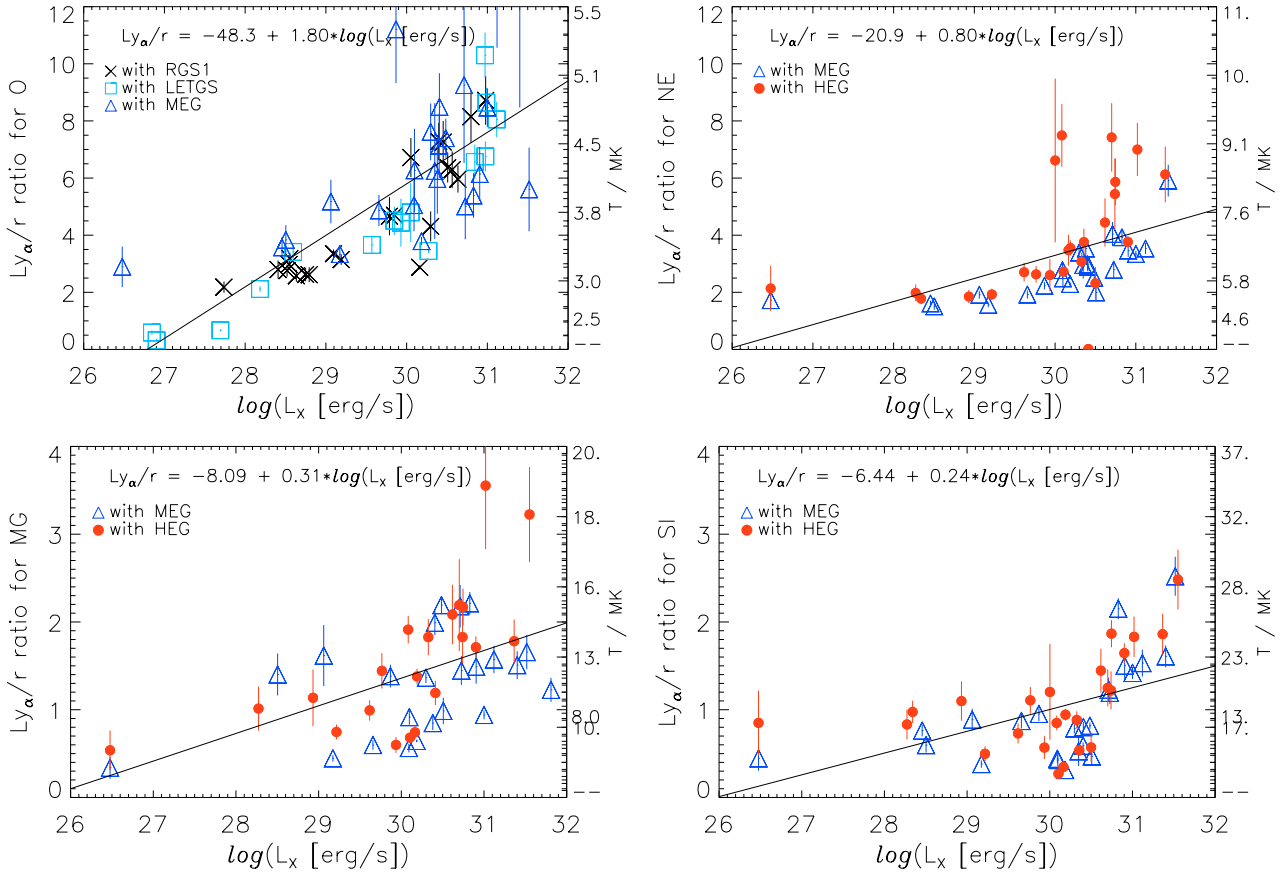

Fig. 4. Line flux ratios of H-like (Ly$_\alpha$) and He-like (r) lines vs. activity indicator L_X for the respective ions of oxygen, neon, magnesium, and silicon. Linear fits yield good approximations with decreasing slopes for higher-Z ions. The right axes give average temperatures derived from comparison of the measured line ratios with temperature-sensitive predictions from the APEC line database.

below one for all the stars in our sample. In plasmas with densities exceeding $n_e = 10^{13.5}$ cm^{-3}, the 121.21 Å is expected to be the strongest Fe XXI line, yet it is detected in none of our sample stars. The "best" cases for detection are the LETGS spectra of Algol and Capella (see Fig. 5 left panel), but the statistical significance of the "features" appearing at 121.21 Å is very low. Even if these features are taken as real, the measured line fluxes do not imply densities higher than 10^{12} cm^{-3}. We also investigated the Fe XXI lines at 142.16 Å and at 145.65 Å for Capella, which were used by Dupree et al. (1993). They measured flux ratios with EUVE λ142.16/λ128.73 = 0.51 and λ145.65/λ128.73 = 0.24 implying densities $\log n_e = 13.2$ and 12.8, but we are unable to detect any significant flux at these wavelengths in the LETGS spectrum of Capella. The grey shaded areas in Fig. 5 show the expected spectrum using the line counts for the 128.73 Å line and the EUVE flux ratios; it can be seen that such high densities would have been measurable with the LETGS.

In Fig. 6 we plot the line flux ratios measured for our sample stars between the detected Fe XXI lines at 117.5 Å, 102.22 Å, and 97.87 Å, all with respect to the Fe XXI line at 128.73 Å. To convert line counts into fluxes we used the effective areas and ISM transmissions listed in Table 3. Note that we did not consider individual ISM transmissions for each star; since this effect is small and differential; the error is smaller than the statistical error of our measurements. The grey lines in Fig. 6 represent the line flux ratios computed from APEC for the case of a low density plasma. As can be seen from Fig. 6 all the ratios for 117.5 Å/128.73 Å are above the computed low density limit, however, all the observed line ratios are consistent with a value of 0.25. Since we consider it unlikely that all observed coronae are above the low-density limit at the same density, a far more plausible explanation is that all coronae are in the low-density limit and that a flux ratio of 0.25 is a more appropriate value for the low-density limit than the computed value of 0.16. Similar conclusions apply to the flux ratios of the 102.2 Å/128.73 Å and 97.87 Å/128.73 Å lines, where the computed low-density values are 0.17 and 0.07, which has to be compared to the observed values of 0.25 and 0.10. Again, the most plausible explanation is that all coronae are in the low density limit, which is consistent with the non-detection of the Fe XXI lines at 121.21 Å, 142.16 Å, and 145.65 Å. We also point out that in no case *all* Fe XXI line ratios yield consistent high densities. Individual deviations from the low-density limit could be due to unidentified blending or other uncertainties in the atomic data bases. In particular, inclompleteness of atomic databases result in a bias towards higher densities. Unknown emission lines could mimic high densities when unexpectedly showing up where we expect to see density-sensitive lines. Our conclusion is that densities above 10^{13} cm^{-3} can definitely be ruled out, and densities above 5×10^{12} cm^{-3} appear highly improbable.

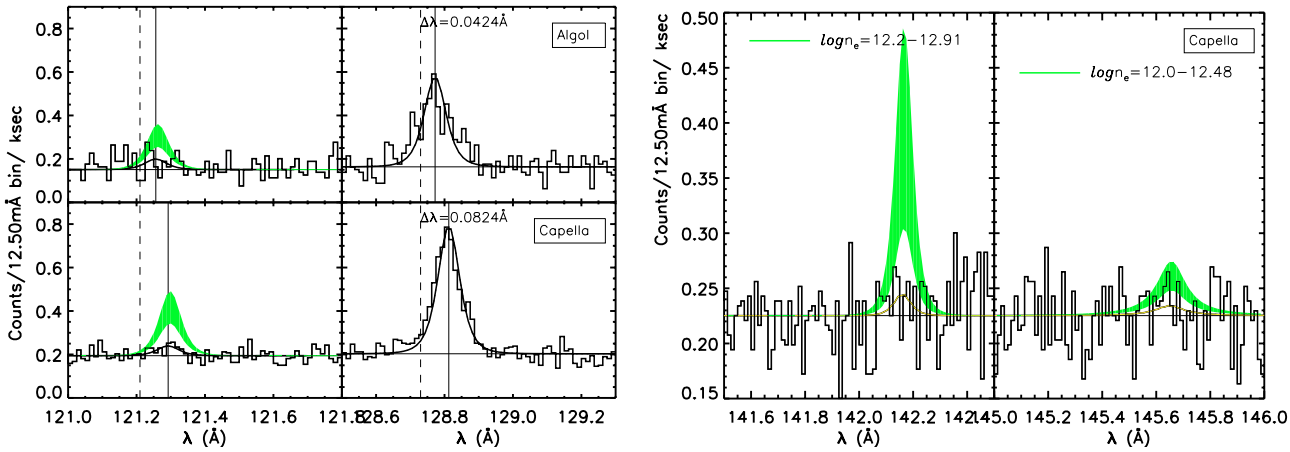

Fig. 5. Measurement of Fe XXI lines for Algol and Capella. At most marginal evidence for the presence of Fe XXI lines at 121.21 Å (*left panel*) and at 142.16 Å as well as 145.65 Å (*right panel*) is present. The 128.73 Å line is shifted due to calibration uncertainties. The grey shaded areas indicate the expected spectrum for high density plasma as found by Dupree et al. (1993).

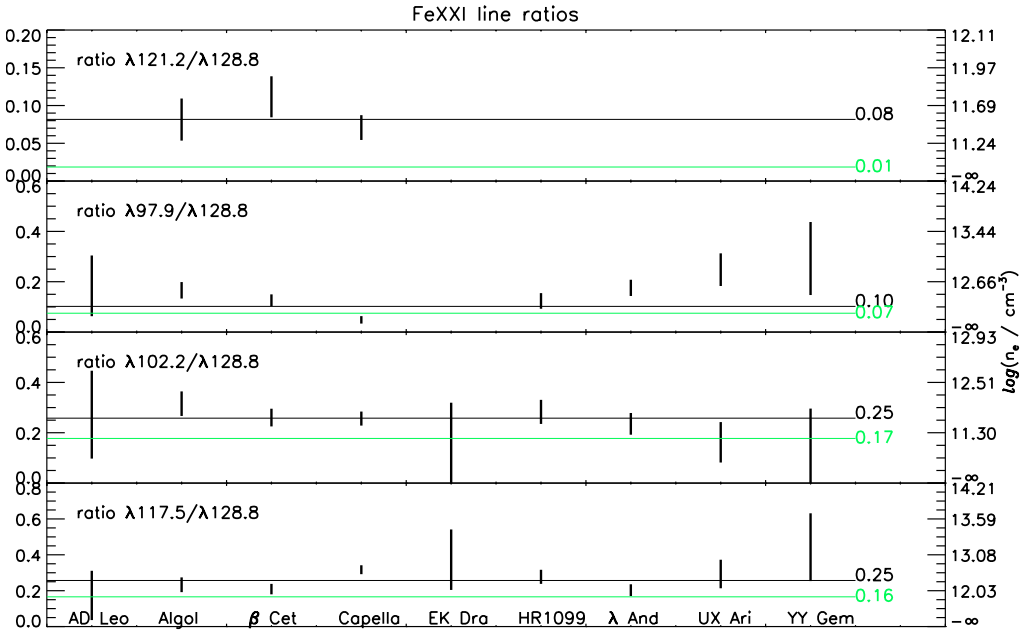

Fig. 6. Line flux ratios for measured Fe XXI lines at 97.9 Å, 102.2 Å, 117.5 Å, 121.21 Å, and 128.8 Å. The grey lines represent the theoretical low-density limits. The average ratios, weighted with the measurement errors, are marked with the black lines.

4.2.2. Densities from He-like lines

Our measurements of line fluxes for O VII and Ne IX lines are used to determine *f*/*i* ratios which are converted to electron densities n_e with Eq. (2); the derived densities (and 1σ higher limits) are listed in Tables A.2 and A.5. The radiation term ϕ/ϕ_c describing the contribution to *f*/*i* ratios from radiatively induced $f \rightarrow i$ transitions is negligible for Ne IX and for O VII for most of our sources. For O VII we calculate ϕ/ϕ_c values for the stars with the highest effective temperatures (cf. Table 2) from IUE measurements at 1630 Å. The method is described in Ness et al. (2001, 2002b). For Algol, Capella, and Procyon we calculate values for ϕ/ϕ_c of 2.18, 0.003, and 0.01, respectively. For Algol the source of UV radiation is the companion B star (Ness et al. 2002c) and depending on the phase geometry during the observation ϕ/ϕ_c can be significantly lower. The density values listed in Tables A.2 and A.5 take radiation effects into account.

4.3. Blending of Ne ix

Specific problems in the measurement of the Ne IX lines arise from the complicated blending structure, studied by Ness et al. (2003a) for Capella using the best SNR data available. According to Ness et al. (2003a) the intercombination line could possibly be blended with an additional line of Fe XIX. Unfortunately this line is only predicted by the APEC line database, but it could not even be resolved with the HEG or in any laboratory measurements. For Capella, Ness et al. (2003a) found this line to contribute to the measured flux with about a third of the total flux measured at 13.55 Å, thus pushing the f/i ratio into the low-density limit (for Capella). When inspecting

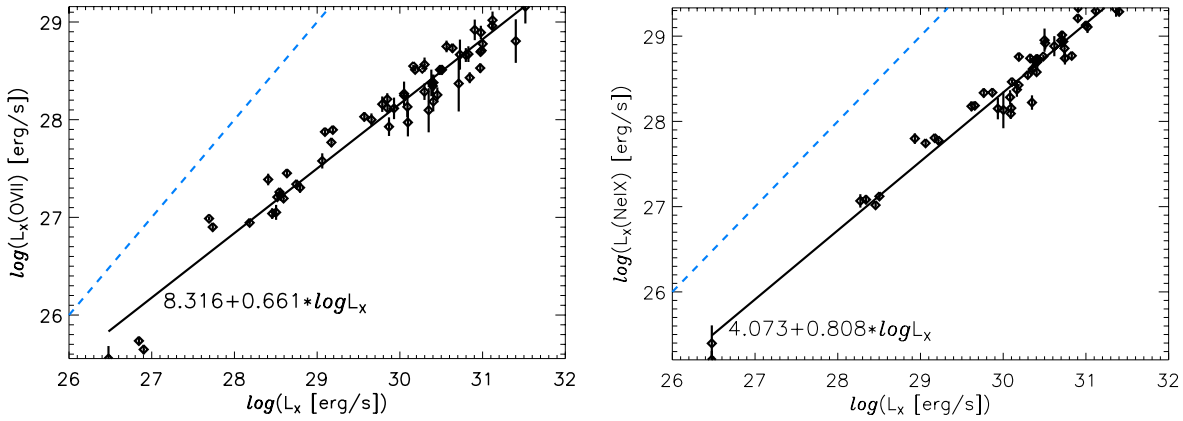

Fig. 7. Comparison of total X-ray luminosity L_X and O VII (*left*) and Ne IX-specific luminosities. The dashed lines indicate lines of equal luminosity.

our Tables A.2 and A.5 we find systematically higher densities from Ne IX line ratios than from O VII line ratios. Since this is critical for the assumption of constant pressure in the X-ray emitting structures, we will test whether systematically higher densities are still found, if the blending is accounted for. We extracted the respective line emissivities from the APEC database and show their temperature dependence in Fig. 8. According to the APEC, blending can be significant at higher temperatures and for larger Fe/Ne abundance ratios (which are rather small for most coronal sources). To assess the amount of expected Fe XIX contamination we adopt a scaling procedure, measuring the line flux of supposedly isolated strong Fe XIX lines and scale with the theoretical ratio of line fluxes.

We extracted emissivities for the Fe XIX line at 13.462 Å and found a value for the ratio of the emissivities and the blending line at 13.551 Å of 8. We then measured line fluxes with the HEG, scaled these with the emissivity ratio 8, and in Table 4 we list line counts thus predicted for the 13.551 Å line. These are contrasted with the original measurements and for most sources higher f/i ratios, yielding lower densities, are indeed found. A similar behavior was found when the 13.518 Å line was used. In Table 5 only sources with particularly high densities are listed, and for Ne IX we calculate densities from the corrected f/i ratios. From Table 5 we conclude that the densities derived from the Ne IX triplet are still systematically higher than those derived from the O VII triplet even if blending is taken into account. Hence the O VII- and Ne IX-emitting layers cannot be at the same pressure. We caution, however, that the blending is purely theoretical and all conclusions rely on the accuracy of the APEC database. Additional blending is predicted to occur from an Fe XX line (see Fig. 8), but we did not make estimates for the contribution from this line, because no Fe XX lines are available for a scaling procedure. For further analysis we use the non-corrected f/i ratios for Ne IX.

4.4. Activity indicators for oxygen and neon

As an activity indicator specific only for the O VII and Ne IX emitting layers we calculate an ion-specific X-ray luminosity from the sum of the three He-like line fluxes r+i+f as described by Ness et al. (2003b). These luminosities are plotted

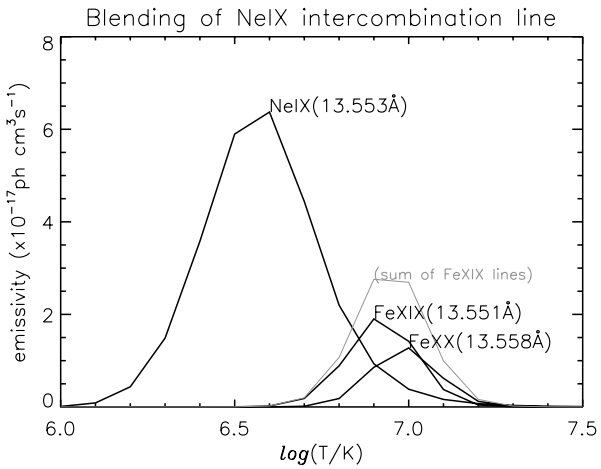

Fig. 8. Iron lines blending the Ne IX intercombination line in high-temperature plasmas predicted by the APEC database assuming solar elemental abundances.

in Fig. 7 in comparison with the total X-ray luminosities (also taken from Ness et al. 2003b and listed in Tables A.1 and A.4). Clearly, the O VII and Ne IX luminosities strongly correlate with the total X-ray luminosity and we conclude that these luminosities represent the overall degree of magnetic activity of the coronae at least as well as the total X-ray luminosities. This is supported by our finding that the average temperatures derived from the respective ions correlate with the overall X-ray luminosity. We find that for the least active stars O VII emission contributes on average less than 10% to the overall luminosity and Ne IX emission at most 7% for stars of intermediate activity. For the active stars the percentage drops to below 3% for oxygen and neon. From the ion-specific luminosities we can also calculate ion-specific emission measures, but a temperature structure has to be assumed for this procedure. For simplicity we assume an isothermal plasma at the peak formation temperature for each ion ($T_{\rm OVII}$ = 2 MK and $T_{\rm NeIX}$ = 4 MK). Note that the emission peak around the He-like ions is very narrow. The ion-specific emission measure is then calculated from

$$EM_{\rm ion} = \frac{L_{\rm X,ion}}{p_\lambda(T_{\rm m})} \qquad (3)$$

Table 4. Blending prediction of Ne IX intercombination line for HEG (first lines) and MEG (second lines).

Star	cts[a]	i [cts]	f [cts]	new f/i	old f/i
24 UMa	1.18	8.83	13.64	1.86	1.61
MEG	4.98	17.19	80.49	6.87	5.14
44 Boo	4.43	40.76	84.48	2.42	2.17
MEG	6.03	132.90	352.56	2.89	2.91
AB Dor	4.14	33.50	77.68	2.76	2.42
MEG	13.09	137.61	290.84	2.43	2.32
AD Leo	2.75	12.77	26.91	2.80	2.20
MEG	4.40	53.71	171.40	3.62	3.50
Algol	2.81	35.73	53.05	1.68	1.55
MEG	20.04	150.82	236.96	1.89	1.72
AR Lac	2.30	10.09	13.90	1.86	1.44
MEG	4.98	48.98	140.80	3.33	3.15
AU Mic	1.02	24.99	52.33	2.27	2.19
MEG	5.81	78.25	214.19	3.08	3.00
β Cet	4.81	32.41	64.72	2.44	2.09
MEG	22.87	127.79	211.92	2.10	1.82
Canopus	0.67	4.68	13.03	3.39	2.91
MEG	3.37	23.29	42.20	2.21	1.99
Capella	35.05	190.47	373.48	2.50	2.05
MEG	105.42	709.92	1373.17	2.37	2.12
ER Vul	4.01	16.96	32.71	2.63	2.02
MEG	9.97	51.41	168.72	4.24	3.60
EV Lac	2.73	24.32	68.82	3.32	2.96
MEG	6.75	85.95	222.32	2.92	2.84
HR 1099	6.13	100.55	228.75	2.52	2.38
MEG	22.02	304.42	834.17	3.08	3.01
II Peg	2.21	19.99	46.00	2.70	2.41
MEG	2.03	103.95	268.87	2.75	2.84
IM Peg	1.89	12.86	30.64	2.91	2.49
MEG	7.41	49.64	127.99	3.16	2.83
λ And	2.51	12.84	35.64	3.59	2.90
MEG	11.26	81.33	219.34	3.26	2.96
μ Vel	3.13	24.12	31.65	1.57	1.37
MEG	8.75	50.20	59.62	1.50	1.30
Prox Cen	0.24	2.93	12.81	4.95	4.57
MEG	0.97	5.54	18.02	4.11	3.57
σ^2 CrB	15.30	88.11	130.60	1.87	1.55
MEG	28.83	296.10	521.80	2.03	1.93
Speedy Mic	0.22	2.77	10.59	4.32	3.99
MEG	0.68	11.57	37.35	3.57	3.54
TY Pyx	1.09	7.09	16.96	2.95	2.50
MEG	5.05	26.51	72.69	3.53	3.01
UX Ari	1.38	7.99	18.57	2.93	2.43
MEG	9.39	120.16	237.38	2.23	2.17
V824 Ara	4.82	29.84	66.01	2.75	2.31
MEG	18.54	157.09	298.00	2.24	2.08
ξ UMa	2.74	29.59	81.17	3.15	2.87
MEG	10.77	138.57	354.90	2.89	2.81

[a]Prediction of blend in i-line from 13.462 Å line.

with $p_\lambda(T_\mathrm{m})$ being the emissivity taken from the APEC database at the peak formation temperature T_m. Here we assume solar photospheric abundances, but for each element the ion-specific emission measure will linearly increase with increasing elemental abundance relative to solar. The emission measures thus obtained are listed in Tables A.1 and A.4.

Table 5. Coronae with lowest measured f/i ratios (oxygen: $f/i <$ 2.2, neon: $f/i < 2.0$). (H = HEG, M = MEG); for neon the predicted blending is taken into account (Sect. 4.3)

		O VII		Ne IX	
Star	Instr.	f/i	$\log(n_\mathrm{e})$ [cm^{-3}]	f/i	$\log(n_\mathrm{e})$ [cm^{-3}]
44 Boo	M	1.69 ± 0.42	10.6 ± 0.19	2.89 ± 0.39	11.0 ± 0.50
	H	–	–	2.42 ± 0.47	11.4 ± 0.32
Algol	M	0.69 ± 0.19	10.9 ± 0.29	1.89 ± 0.22	11.7 ± 0.11
	H	–	–	1.68 ± 0.39	11.8 ± 0.19
EV Lac	M	1.52 ± 0.33	10.7 ± 0.15	2.92 ± 0.41	11.0 ± 0.60
	H	–	–	3.32 ± 0.73	<11.5
II Peg	M	1.49 ± 0.40	10.7 ± 0.20	2.75 ± 0.41	11.2 ± 0.40
	H	–	–	2.70 ± 0.66	11.2 ± 0.83
μ Vel	M	7.24 ± 5.24	<11.5	1.50 ± 0.31	11.8 ± 0.16
	H	–	–	1.57 ± 0.40	11.8 ± 0.21
σ^2 CrB	M	2.07 ± 0.39	10.4 ± 0.17	2.03 ± 0.17	11.6 ± 0.08
	H	–	–	1.87 ± 0.22	11.7 ± 0.11
TY Pyx	M	1.29 ± 0.76	10.8 ± 0.49	3.53 ± 0.89	<12.2
	H	–	–	2.95 ± 1.29	<12.0
V824 Ara	M	1.51 ± 0.46	10.7 ± 0.23	2.24 ± 0.25	11.5 ± 0.13
	H	–	–	2.75 ± 0.54	11.2 ± 0.63

5. Structure of oxygen and neon emitting layers

Figure 11 (for O VII) and Fig. 12 (for Ne IX) show the central results of our measurements in graphical form. In the upper panels of these figures we show the measured f/i ratios and the densities derived with these measurements with Eq. (2) vs. the ion-specific luminosities ($L_\mathrm{X,O\,VII}$ and $L_\mathrm{X,Ne\,IX}$). The low-density limit R_0 is marked with a vertical dotted line in the upper left panels, only measurements with f/i-ratios $<R_0$ yield actual density measurements. Therefore all f/i measurements resulting in low-density limits have been marked by light colors. In the bottom left panels we plot the densities versus the emission measure obtained from the ion-specific luminosities calculated with Eq. (3). In the plot we include lines of equal emitting (coronal) volumes V_cor derived from

$$EM_\mathrm{ion} = 0.85\, n_\mathrm{e}^2 V_\mathrm{cor}\,. \quad (4)$$

The coronal volumes derived from the O VII densities and the Ne IX densities are consistent with each other. This is demonstrated in Fig. 9, where the bulk of measured volumes does not depart significantly from the line of equal volumes.

For each ion we estimate available volumes V_avail, which can potentially be filled with coronal plasma. We use stellar radii (cf. Table 2) and a scale height H: $V_\mathrm{avail} = 4\pi R_\star^2 H$ (terms of $R_\star H^2$ and H^3 are neglected) and compare V_avail with the ion specific emitting volumes. For an estimate of the height we assume the plasma to be confined in a uniform distribution of loop structures obeying the loop scaling law by Rosner et al. (1978, RTV):

$$n_\mathrm{e,hot} L = 1.3 \times 10^6 T_\mathrm{hot}^2 \quad (5)$$

with the electron density $n_\mathrm{e,hot}$ and the plasma temperature T_hot at the loop top. While emitting volumes can be derived only from the densities (Eq. (4)), we additionally need the plasma

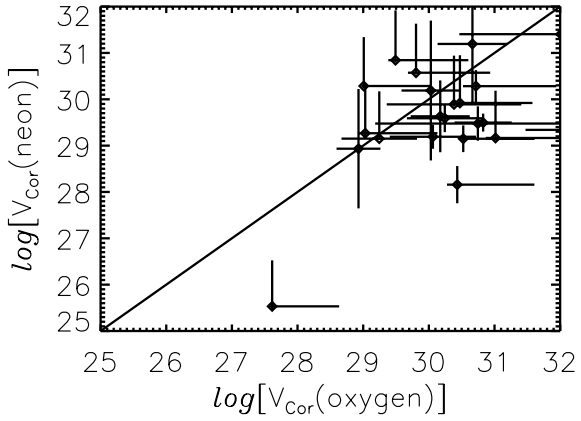

Fig. 9. Comparison of coronal volumes obtained from O VII and Ne IX (only MEG measurements). The solid line marks the line of equal volumes.

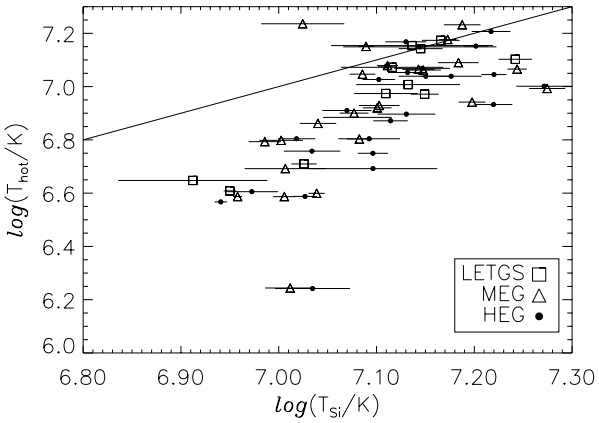

Fig. 10. Comparison of temperatures derived from Eq. (6) and from Si H-like and He-like line ratios representing the hot component for those stars where HETGS and LETGS spectra are available.

temperature to estimate loop lengths L. As a first approach we use the temperatures derived from the H-like and He-like lines of the respective ions from which the densities are derived. This implies that the ion-specific temperature estimate represents the overall corona, which is certainly not true for the more active stars. Nevertheless, the loop lengths derived from the oxygen and neon temperatures can be regarded as lower limits. Our second approach is based on finding a loop-top temperature $T_{\rm hot}$ that scales with the X-ray luminosity. We regard the loop-top temperature as equivalent to the hotter component of a two-temperature distribution as found by Güdel et al. (1997). The temperature $T_{\rm hot}$ we therefore derive from the X-ray luminosity using Eq. (1). Since Güdel et al. (1997) had only solar like stars in their sample we scale the relation to the different stellar radii, thus using surface fluxes instead of luminosities:

$$T_{\rm hot}^4 = \frac{L_{\rm X}}{55}\left(\frac{R_\star}{R_\odot}\right)^{-2}. \quad (6)$$

For binary stars we use the stellar radius of the component assumed to be more active. We tested the consistency of these temperatures with line-based hot temperatures determined from the H-like and He-like Si lines measured with the HETGS and the LETGS and estimated plasma temperatures with the APEC line database. From Fig. 10 it can be seen that in particular for the most active of our sample stars these temperatures agree quite well, while for somewhat less active stars some emission measure is still present at high temperature and the bulk of the emission measure is at a lower temperature. The density at the loop-top (i.e., of the hot component) $n_{\rm e,hot}$ we derive from the measured densities $n_{\rm e}$(O VII) and $n_{\rm e}$(Ne IX) assuming pressure equilibrium, i.e., $n_{\rm e}T_{\rm ion} = n_{\rm e,hot}T_{\rm hot}$.

From these considerations we derive the available volume

$$V_{\rm avail} \stackrel{(a)}{=} 4\pi R_\star^2 L \stackrel{(b)}{=} \frac{4\pi\, 1.3\times10^6\, R_\star^{1/2} R_\odot^{3/2}}{n_{\rm e}T_{\rm ion}}\left(\frac{L_{\rm X}}{55}\right)^{3/4} \quad (7)$$

in cgs units. The values we derived for $V_{\rm cor}$ and $V_{\rm avail}$ are listed in Tables A.3 and A.6 and we plot these volumes in the bottom right panels of Figs. 11 and 12. In addition we plot a line of equal volumes and it can be seen that the derived coronal volumes are significantly lower than the available volumes. One has to keep in mind that here only the O VII and Ne IX emitting regions contribute to the coronal volume while the available volume represents the maximal extent of the corona derived from its degree of activity. The ratio of these volumes is defined as the filling factor

$$f = \frac{V_{\rm cor}}{V_{\rm avail}}, \quad (8)$$

and we plot the derived filling factors versus activity in Fig. 13. The values obtained for the filling factors are given in Tables A.3 and A.6. Upper estimates of filling factors are calculated by using the temperatures derived from the ratios of H-like and He-like lines in Eq. (5) as $T_{\rm hot}$. Since these temperatures are lower than the temperatures derived from Eq. (6), the estimated loop lengths and thus the available volumes as calculated with Eq. (7) (a) will be smaller. Therefore an upper limit is found for the filling factors, and those are marked with red bullets in Fig. 13, while all other quantities are based on the temperatures from Eq. (6).

6. Discussion and conclusions

For inference of sizes in stellar coronae the scaling laws derived for the solar corona can be used to link physical properties with spatial sizes under the assumption of loop-like geometries as identical building blocks. The physical parameters required for the application of the scaling laws are the plasma temperature, emission measure, and density. While good estimates of plasma temperatures and emission measures are available from low-resolution spectroscopy, estimates of plasma density do require high-resolution spectroscopy. The He-like triplets provide a direct way to measure densities by using collisionally induced reduction of the so-called *f*/*i* line flux ratio with increasing plasma density. The density-sensitive regimes of the different He-like ions increase with atomic number and the best measurable density range is provided by the O VII triplet and the Ne IX triplet. The N VI and C V triplets are also good density tracers; however, the lines of both are quite faint. C V can only be measured with the LETGS and can be blended with Ne IX/Fe XIX third

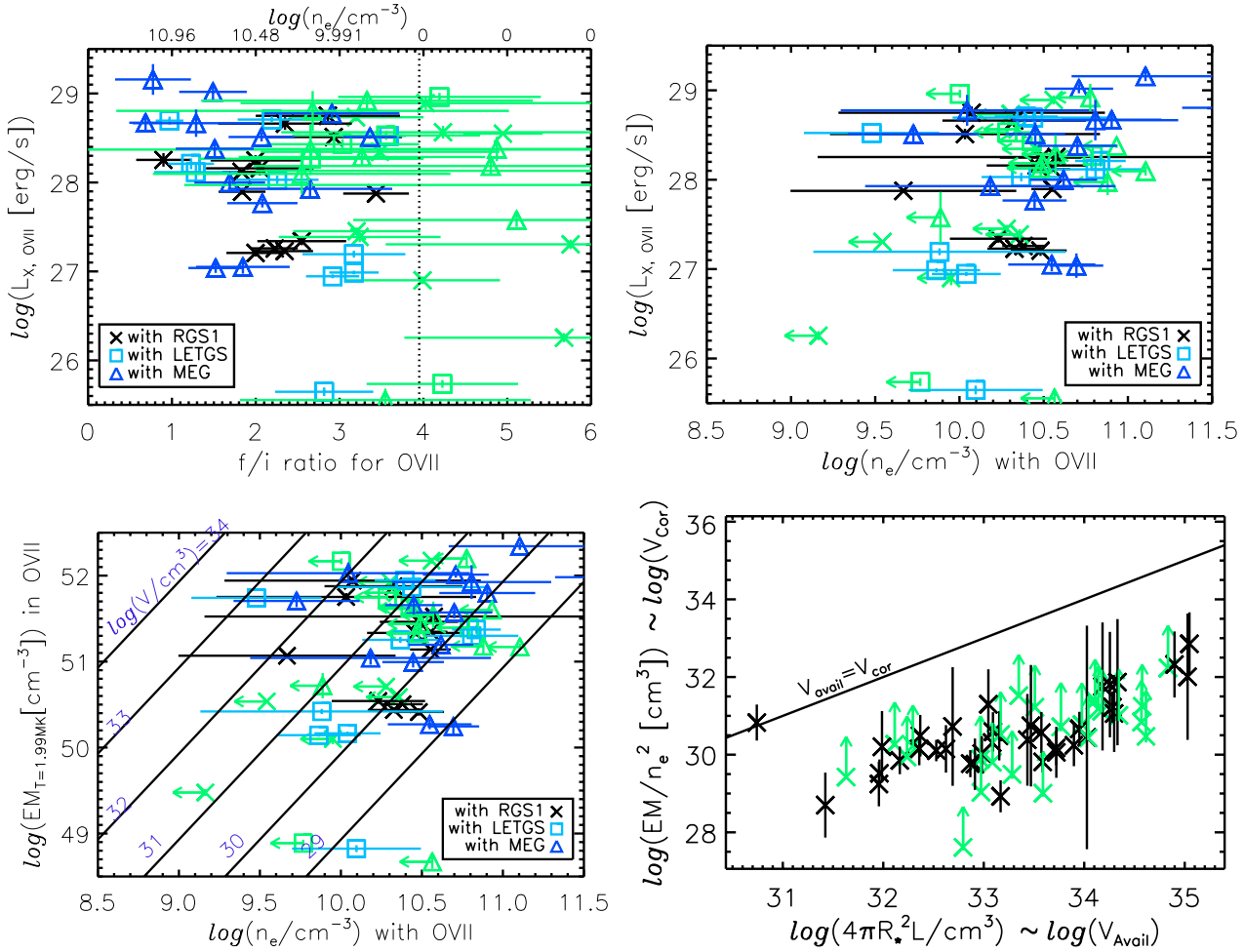

Fig. 11. Measured f/i ratios and derived densities versus the O VII specific X-ray luminosities (*upper two panels*). The low-density limit is marked with a vertical dotted line and measurements with only upper limits are marked by light symbols. *Lower left panel*: densities versus O VII specific emission measure at $T = 2$ MK. *Lower right*: emitting volume versus available volume (Eq. (7) with $T_{\rm hot}$ from Eq. (6); numbers are listed in Tables A.2/A.5, A.1/A.4, and A.3/A.6).

order lines for the more active stars (Ness et al. 2001). The ions of C V and N VI are produced at rather low temperatures and therefore probe only the cooler coronal plasma. The O VII triplet is very prominent and can be measured by all grating instruments with high precision, but again it represents only the low-temperature regions of a multi-temperature plasma. The Ne IX triplet is sensitive to somewhat higher densities and is produced at higher temperatures than O VII. However, the measurement of Ne IX is difficult because of Fe XIX lines blending with the Ne IX lines, particularly the important intercombination line (Ness et al. 2003a). The most reliable results on the Ne IX lines can therefore be derived from the HETGS data for the Ne IX f/i ratios.

The results of our density measurements can be summarized as follows: first, for O VII the measured *f/i*-ratios are in the range ≈1 to the low density limit of 3.95. The coronal source with the hitherto lowest measured O VII *f/i*-ratio is Algol, which yields $f/i \sim 1$ for RGS, LETGS, and MEG data, i.e., in three independent measurements. While Algol is indeed very active, it is in our opinion very likely that these low f/i-values are affected by the radiation field of Algol's primary. This is supported by the lack of such low f/i-ratios for Ne IX (for higher-Z He-like ions the effects from UV radiation fields become lower; cf. Fig. 8 in Ness et al. 2002d). Second, for Ne IX the measured f/i-ratios are in the range ≈1 to the low density limit of 3.4. A handful of stars like 44 Boo, Algol, AR Lac, and EV Lac have the lowest values, but discrepancies appear between measurements with different instruments and even between simultaneous measurements (in MEG and HEG). Third, in no case do we have significant density measurements from Fe XXI. Although all measured line ratios should yield consistent densities, we found that none of our spectra returned consistently high densities. We further found no detections for lines that typically appear in high density plasmas. From the upper limits of our Fe XXI density estimates the typically encountered densities in coronal plasmas are definitely not higher than 5×10^{12} cm^{-3}. Therefore the Si XIII and the Mg XI triplets will yield only low-density limits in coronal plasmas. Recent systematic studies of Si and Mg He-like f/i ratios by Testa et al. (2004) indeed revealed only low-density limits for Si XIII for all stars in their sample, but some density measurements for Mg XI are also

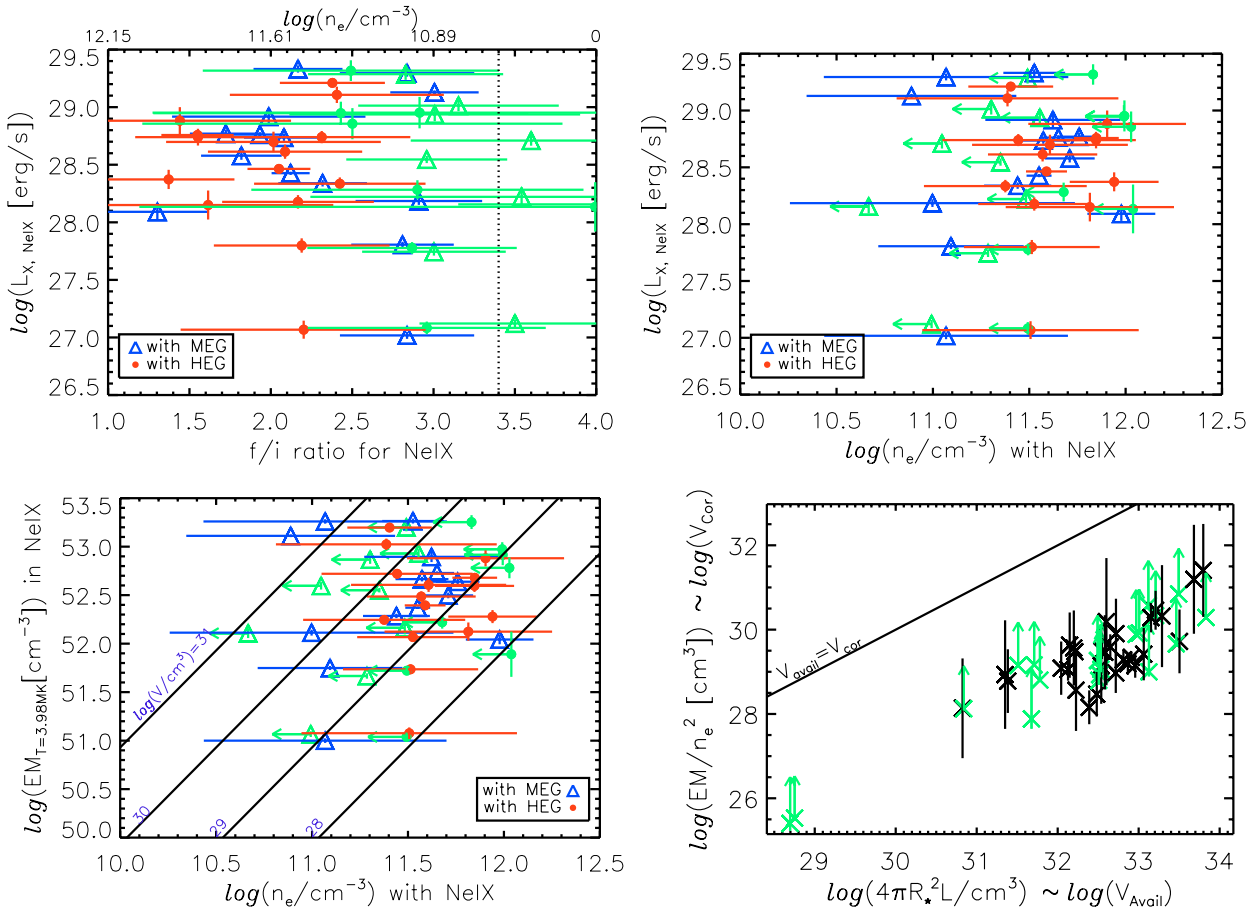

Fig. 12. Same as Fig. 11 for Ne IX.

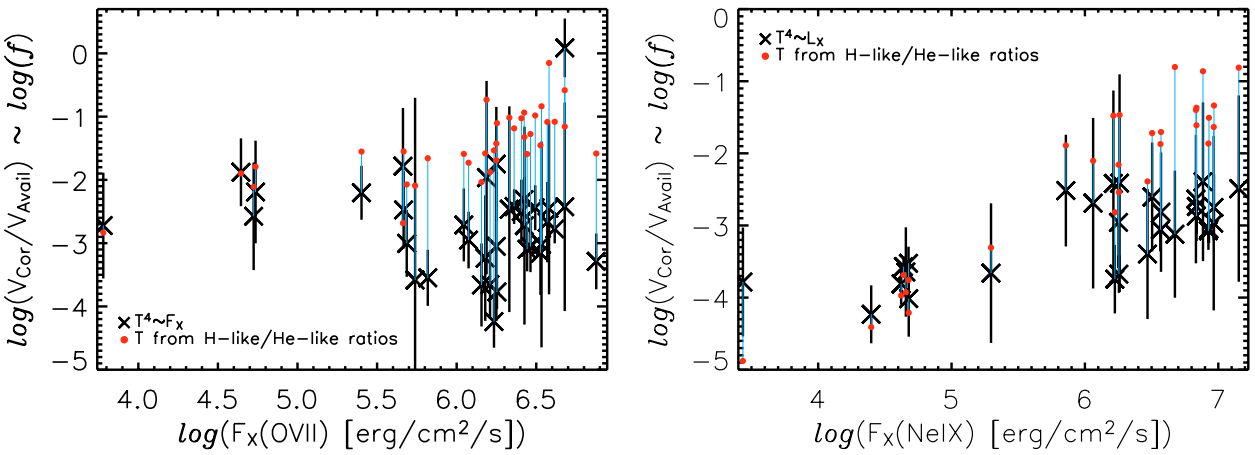

Fig. 13. Filling factors obtained from ratios of coronal volumes (derived from O VII and Ne IX densities) and assumed available volumes. The latter depend on assumed loop-top temperatures, which we derive from the H-like and He-like line ratios (marked with red bullets) and from L_X (Eq. (6)). As activity indicator we use here the surface fluxes F_X from $L_X(\mathrm{ion})/(4\pi R_\star^2)$.

reported. Deviations from the Si f/i low-density limit (systematically higher f/i values as expected) were argued to imply too low a theoretical low-density f/i value. Testa et al. (2004) point out that densities in stellar coronae do not exceed $\log n_e = 13$ as reported by, e.g., Sanz-Forcada et al. (2003b) for AB Dor. The deviations found for Mg f/i ratios were found to be related to the ratio of X-ray luminosity and bolometric luminosity, but no discernible trend with the X-ray surface flux was found. A particular difficulty was that the Mg XI lines are blended with lines of the Ne Ly series ($n > 5$), increasing the formal measurement errors. Testa et al. (2004) successfully disentangled the lines, but admit that residual Ne blending might still be present.

It is instructive to inspect the "low" f/i-ratios for O VII and Ne IX where measurements with good SNR and high resolution (i.e., MEG) are available. In Table 5 we list only those measurements where the oxygen f/i-ratios are below 2.2 (within the errors) and the neon f/i-ratios are below 2.0. The

peculiar role of Algol becomes apparent; its low O VII f/i-ratio stands out, while the Ne IX f/i-ratio does not. The densities derived from O VII and Ne IX usually differ, the Ne IX densities being higher than the corresponding O VII densities. However, using the MEG values the densities for 44 Boo, EV Lac, and II Peg are consistent, while they are inconsistent for the RS CVn stars Capella and σ CrB. The case of Capella appears especially striking: While three different measurements (with RGS, LETGS, MEG) yield consistent "high" values of the O VII f/i-ratio, both MEG and HEG yield consistent "low" values for the Ne IX f/i-ratio. The Ne IX measurement for Capella has been discussed in great detail by Ness et al. (2003a) and it was found that the intercombination line could be blended with an additional Fe XIX line that cannot be resolved with MEG and HEG. In the case of Capella it turned out that accounting for the predicted amount of blending leads to the low-density limit, thus to densities consistent with the densities obtained from O VII. We note that the densities (for Capella) derived from Ne IX are fully consistent with the upper limits derived from Fe XXI (even without accounting for theoretically predicted blending); at any rate, the case of Capella (and possibly that of σ CrB) appears somewhat peculiar.

With the measured densities of the cool and hot plasma component we computed the emitting volumes of these plasma components (cf. Tables A.3 and A.6). Surprisingly, these volumes are rather small, for the "best" data sets with the smallest errors one finds volumes between 10^{29}–$10^{30.5}$ cm^3 for O VII and somewhat smaller values for Ne IX. For example, for EV Lac we find $V_{\rm cor} = 10^{28.9}$ cm^3 for oxygen and neon; assuming a filling factor of unity, one would obtain a coronal scale height of 100 km, which appears pathologically small. We therefore conclude that the filling factor is far away from unity, and that conclusion is substantiated by more sophisticated calculations of the coronal volume. We first calculated the volume of a maximum corona consisting of hydrostatic loops with isothermal temperatures derived from the Ly$_\alpha$/He-like line ratios for the respective ions and the measured density, and second, computed maximal coronal volumes from the relationship between the temperature of the hotter plasma and the total stellar X-ray luminosity reported by Güdel et al. (1997) and, again, find small overall filling factors.

So far, the discussion assumed isolated temperature components. Under reasonable physical conditions one expects the pressure to stay approximately constant along any magnetic field line since the high observed temperatures imply large pressure scale heights. Under this assumption the high-density Ne IX emission regions cannot be magnetically connected with the high-density O VII emission regions because the Ne densities would have to be below the O densities, the opposite of what is observed. On the other hand, assuming isobaric loops, any loop emitting in Ne IX will also emit in the O VII lines; also, the density of these O VII layers will be even larger than those of the Ne IX emission layers. Therefore the observed O VII emission would have to be composed of at least two components, a high-temperature, high-density component, which contributes rather little to the observed flux in the forbidden O VII line, and a lower-temperature, lower-density component, which contributes to the bulk of the forbidden O VII line. A detailed modeling in terms of physically consistent loops is beyond the scope of this paper; here, we just consider the following numerical example of EV Lac. The observed ratios of the fluxes of the He-r line of Ne IX and the Ly$_\alpha$ lines imply temperatures of about log$T \approx 6.7$, the observed Ne *f*/*i*-ratio of 2.92 implies densities of about $10^{11.1}$ cm^{-3}. The O VII emission would then be located at a density of $10^{11.6}$ cm^{-3}, which in turn would lead to an O VII *f*/*i*-ratio of 0.29 for this material. Decomposing the observed O VII f and i emission into a "hot" component (with $f/i = 0.29$) and a "cool" component (with an assumed low-density limit of $f/i = 3.95$), so that the overall f/i-ratio is equal to the observed *f*/*i*-ratio of 1.52, leads to the following numbers: $f_{\rm c} = 46.6$, $i_{\rm c} = 11.8$, $f_{\rm h} = 8.3$, $i_{\rm h} = 28.5$, i.e., a situation where the f-line is dominated by the low-pressure component, but the i-line by the high-pressure component. The filling factor of the low-pressure component is undetermined and could be large, while the filling factor of the high-pressure component, which contributes most of the flux, would definitely be quite small and dominant by virtue of its high density.

What, then, do we learn about coronal structure? First, an inactive corona is generally dominated by cool plasma (1–4 MK), and this plasma never covers a large fraction of the surface as is the case for the non-flaring Sun. For active stars, cool plasma might actually cover a larger fraction of the stellar surface, but more strikingly, a hot component appears. This hot component has been known since the earliest stellar X-ray observations, but its nature has been debated. Its characteristic temperature seems to be correlated with the activity level, and in extremely active stars it reaches temperatures that on the Sun are known exclusively during flares. In our investigation, we cannot confine the extent of the hot plasma because we do not find conclusive indications for a definitive density of this plasma component. We rather argue that we measure upper limits. Yet we have added two further pieces of information: first, the cooler plasma component cannot cover a large fraction of the stellar surface. And second, there must be spatially separate plasma components at different temperatures (e.g., those detected by the O VII and the Ne IX density analysis). We tentatively argue that the hotter plasma loops fill the space between cooler loops until much of the corona is dominated by the hot plasma. Why, then, do hot loops become progressively more important as the stellar activity increases? As the magnetic activity level and consequently the surface magnetic filling factor increases, the coronal magnetic fields become denser, leading to increased interactions between neighboring field lines, which leads to increased heating (Güdel et al. 1997). The increased heating rate inevitably drives chromospheric material into the loops until an equilibrium is attained. The X-ray luminosity of the hot plasma thus rapidly increases as we move to more active stars. In their most extreme form, such interactions lead to increased levels of flaring, again resulting in increased amounts of hot, luminous plasma. In this picture, the cooler loops are post-flare loops that are still over-dense while returning to their equilibrium state.

Whatever the cause for the increased heating, a relatively cool component, corresponding to typical active regions as seen on the Sun, appears to be present in all stars at

a similar level of surface coverage. Our survey has shown that this component reveals densities that may exceed 10^{10} cm^{-3} but a clear systematic trend with the overall activity level does not seem to be present.

Acknowledgements. This work is based on observations obtained with Chandra and XMM-Newton, an ESA science mission with instruments and contributions directly funded by ESA Member States and the USA (NASA). This research has made use of the SIMBAD database, operated at CDS, Strasbourg, France. J.-U.N. acknowledges financial support from Deutsches Zentrum für Luft- und Raumfahrt e.V. (DLR) under 50OR98010. AT and MG acknowledge support from the Swiss National Science Foundation (grant No. 2000-066875).

References

Abbott, M. J., Boyd, W. T., Jelinsky, P., et al. 1996, ApJS, 107, 451
Arnaud, M., & Rothenflug, R. 1985, A&AS, 60, 425
Audard, M., Behar, E., Güdel, M., et al. 2001, A&A, 365, L329
Blumenthal, G. R., Drake, G. W. F., & Tucker, W. H. 1972, ApJ, 172, 205
Bowyer, S., Drake, J. J., & Vennes, S. 2000, ARA&A, 38, 231
Dere, K. P., Landi, E., Young, P. R., & Del Zanna, G. 2001, ApJS, 134, 331
Dupree, A. K., Brickhouse, N. S., Doschek, G. A., Green, J. C., & Raymond, J. C. 1993, ApJ, 418, L41
Güdel, M., Schmitt, J. H. M. M., Benz, A. O., & Elias, N. M. 1995, A&A, 301, 201
Güdel, M., Guinan, E. F., & Skinner, S. L. 1997, ApJ, 483, 947
Güdel, M., Audard, M., Briggs, K., et al. 2001, A&A, 365, L336
Güdel, M., Arzner, K., Audard, M., & Mewe, R. 2003, A&A, 403, 155
Gabriel, A. H., & Jordan, C. 1969, MNRAS, 145, 241
Güdel, M. 2004, in A&AR, submitted
Hünsch, M., Schmitt, J. H. M. M., Sterzik, M. F., & Voges, W. 1999, A&AS, 135, 319
Kaler, J. B. 1989, Stars and their spectra. An introduction to spectral sequence (Cambridge: Cambridge University Press)
Linsky, J. L., Wood, B. E., Brown, A., & Osten, R. A. 1998, ApJ, 492, 767
Mason, H. E., Doschek, G. A., Feldman, U., & Bhatia, A. K. 1979, A&A, 73, 74
Mewe, R., Raassen, A. J. J., Drake, J. J., et al. 2001, A&A, 368, 888
Ness, J.-U., Mewe, R., Schmitt, J. H. M. M., et al. 2001, A&A, 367, 282
Ness, J.-U., Mewe, R., Schmitt, J. H. M. M., & Raassen, A. J. J. 2002a, in Stellar Coronae in the Chandra and XMM-NEWTON Era, ASP Conf. Ser., 277, 545
Ness, J.-U., Mewe, R., Schmitt, J. H. M. M., & Raassen, A. J. J. 2002b, in The Future of Cool-Star Astrophysics, 2003, ed. A. Brown, G. M. Harper, & T. R. Ayres, Proc. 12th Cambridge Workshop on Cool Stars, Stellar Systems, and The Sun, 255
Ness, J.-U., Schmitt, J. H. M. M., Burwitz, V., Mewe, R., & Predehl, P. 2002c, A&A, 387, 1032
Ness, J.-U., Schmitt, J. H. M. M., Burwitz, V., et al. 2002d, A&A, 394, 911
Ness, J.-U., Brickhouse, N. S., Drake, J. J., & Huenemoerder, D. P. 2003a, ApJ, 598, 1277
Ness, J.-U., Schmitt, J. H. M. M., Audard, M., Güdel, M., & Mewe, R. 2003b, A&A, 407, 347
Ness, J.-U., & Wichmann, R. 2002, Astron. Nachr., 323, 129
Pallavicini, R., Golub, L., Rosner, R., et al. 1981, ApJ, 248, 279
Porquet, D., Mewe, R., Dubau, J., Raassen, A. J. J., & Kaastra, J. 2001, A&A, 376, 1113
Pradhan, A., & Shull, J. M. 1981, ApJ, 249, 821
Robinson, R. D., Maran, S. P., Carpenter, K. G., Brandt, J. C., & Linsky, J. L. 1994, Bull. Amer. Astron. Soc., 26, 865
Rosner, R., Tucker, W., & Vaiana, G. S. 1978, ApJ, 220, 643
Sanz-Forcada, J., Brickhouse, N. S., & Dupree, A. K. 2003a, ApJS, 145, 147
Sanz-Forcada, J., Maggio, A., & Micela, G. 2003b, A&A, 408, 1087
Schmitt, J. H. M. M. 1997, A&A, 318, 215
Schmitt, J. H. M. M., Collura, A., Sciortino, S., et al. 1990, ApJ, 365, 704
Schmitt, J. H. M. M., Haisch, B. M., & Drake, J. J. 1994, Science, 265, 1420
Schmitt, J. H. M. M., & Kürster, M. 1993, Science, 262, 215
Schmitt, J. H. M. M., & Ness, J.-U. 2004, A&A, 415, 1099
Schrijver, C. J., Mewe, R., & Walter, F. M. 1984, A&A, 138, 258
Siarkowski, M., Pres, P., Drake, S. A., White, N. E., & Singh, K. P. 1996, ApJ, 473, 470
Smith, R. K., Brickhouse, N. S., Liedahl, D. A., & Raymond, J. C. 2001, ApJ, 556, L91
Stelzer, B., & Schmitt, J. H. M. M. 2004, A&A, 418, 687
Testa, P., Drake, J. J., & Peres, G. 2004, ApJ, in press
White, N. E., Shafer, R. A., Parmar, A. N., Horne, K., & Culhane, J. L. 1990, ApJ, 350, 776
Young, P. R., Del Zanna, G., Landi, E., et al. 2003, ApJS, 144, 135

Online Material

Appendix A: Tables

Table A.1. X-ray luminosities, H-like and He-like line fluxes, and ion-specific luminosities and emission measures.

		L_X	Line flux (10^{-13} erg cm^{-2} s^{-1})		$L_{X,O\,VII}$	$L_{X,Ne\,IX}$	log(EM/cm^{-3})	
star	Instr.	[10^{28} erg/s]	O VIII	O VII(r)	[10^{28} erg/s]	[10^{28} erg/s]	O VII[a]	Ne IX[b]
24 UMa	MEG	125.04	2.44 ± 0.16	0.39 ± 0.09	0.94 ± 0.63	1.43 ± 0.40	51.18 ± 0.22	52.11 ± 0.10
	HEG	86.16	–	–	–	1.41 ± 0.83	–	52.12 ± 0.19
44 Boo	MEG	45.35	12.61 ± 0.46	2.59 ± 0.27	1.00 ± 0.30	1.53 ± 0.24	51.20 ± 0.10	52.11 ± 0.06
	HEG	41.36	–	–	–	1.50 ± 0.41	–	52.07 ± 0.10
47 Cas	RGS1	112.88	4.66 ± 0.15	0.69 ± 0.07	1.77 ± 0.50	–	51.46 ± 0.09	–
AB Dor	RGS1	70.87	12.58 ± 0.23	2.68 ± 0.12	1.31 ± 0.17	–	51.35 ± 0.04	–
	MEG	73.87	14.89 ± 0.53	1.33 ± 0.22	0.85 ± 0.37	2.18 ± 0.28	51.04 ± 0.16	52.29 ± 0.05
	HEG	58.21	–	–	–	2.16 ± 0.55	–	52.25 ± 0.09
α Cen A	LETG	0.08	0.32 ± 0.05	1.00 ± 0.09	–	–	48.82 ± 0.08	–
α Cen B	RGS1	0.00	5.27 ± 0.41	4.49 ± 0.40	–	–	49.48 ± 0.08	–
	LETG	0.07	0.69 ± 0.07	1.16 ± 0.10	0.01 ± 0.00	–	48.89 ± 0.08	–
AD Leo	RGS1	3.50	11.59 ± 0.27	3.89 ± 0.17	0.18 ± 0.02	–	50.50 ± 0.04	–
	LETG	3.93	10.94 ± 0.32	3.20 ± 0.21	0.16 ± 0.03	–	50.42 ± 0.06	–
	MEG	3.19	8.70 ± 0.43	2.27 ± 0.28	0.11 ± 0.04	0.13 ± 0.02	50.27 ± 0.12	51.07 ± 0.06
	HEG	1.88	–	–	–	0.12 ± 0.04	–	51.08 ± 0.12
Algol	RGS1	283.73	8.34 ± 0.21	1.15 ± 0.11	1.79 ± 0.63	–	51.52 ± 0.09	–
	LETG	944.99	17.06 ± 0.33	2.53 ± 0.19	4.95 ± 1.03	–	51.87 ± 0.07	–
	MEG	673.63	11.60 ± 0.48	2.15 ± 0.30	4.69 ± 1.75	5.89 ± 0.97	51.80 ± 0.13	52.64 ± 0.06
	HEG	557.72	–	–	–	5.49 ± 1.85	–	52.60 ± 0.12
AT Mic	RGS1	15.47	11.20 ± 0.30	3.56 ± 0.19	0.79 ± 0.12	–	51.14 ± 0.05	–
AU Mic	RGS1	12.43	10.70 ± 0.20	3.19 ± 0.12	0.75 ± 0.07	–	51.07 ± 0.03	–
	MEG	11.52	7.39 ± 0.35	1.43 ± 0.20	0.38 ± 0.14	0.56 ± 0.09	50.72 ± 0.29	51.67 ± 0.06
	HEG	8.55	–	–	–	0.63 ± 0.18	–	51.74 ± 0.10
β Cet	RGS1	198.67	8.49 ± 0.40	1.97 ± 0.22	3.67 ± 1.22	–	51.80 ± 0.10	–
	LETG	699.24	8.63 ± 0.20	1.31 ± 0.12	2.69 ± 0.70	–	51.63 ± 0.08	–
	MEG	253.19	6.10 ± 0.26	0.85 ± 0.13	1.53 ± 0.71	3.79 ± 0.62	51.44 ± 0.13	52.50 ± 0.06
	HEG	227.48	–	–	–	4.11 ± 1.17	–	52.49 ± 0.11
Canopus	MEG	322.00	1.16 ± 0.11	0.30 ± 0.07	6.46 ± 4.70	8.27 ± 2.72	–	52.90 ± 0.11
	HEG	316.10	–	–	–	8.96 ± 5.72	–	52.92 ± 0.21
χ^1 Ori	RGS1	6.21	3.23 ± 0.16	1.23 ± 0.11	0.20 ± 0.05	–	50.54 ± 0.02	–
EK Dra	RGS1	61.25	2.35 ± 0.13	0.50 ± 0.07	1.44 ± 0.53	–	51.33 ± 0.08	–
	LETG	85.01	2.07 ± 0.12	0.47 ± 0.08	1.31 ± 0.67	–	51.30 ± 0.17	–
ϵ Eri	RGS1	0.55	7.13 ± 0.35	3.27 ± 0.25	0.08 ± 0.02	–	50.10 ± 0.12	–
	LETG	1.53	8.04 ± 0.18	3.80 ± 0.15	0.09 ± 0.01	–	50.17 ± 0.04	–
EQ Peg	RGS1	4.31	9.10 ± 0.37	3.53 ± 0.25	0.28 ± 0.06	–	50.71 ± 0.07	–
ER Vul	MEG	240.10	2.57 ± 0.15	0.43 ± 0.08	2.38 ± 1.52	5.13 ± 1.06	51.60 ± 0.25	52.60 ± 0.08
	HEG	258.20	–	–	–	4.99 ± 2.06	–	52.61 ± 0.15
EV Lac	RGS1	3.58	9.19 ± 0.25	2.89 ± 0.16	0.17 ± 0.02	–	50.44 ± 0.06	–
	MEG	2.86	6.64 ± 0.25	1.86 ± 0.17	0.11 ± 0.03	0.10 ± 0.01	50.25 ± 0.03	51.00 ± 0.05
	HEG	2.19	–	–	–	0.12 ± 0.03	–	51.04 ± 0.09
HD 223460	MEG	3289.00	1.82 ± 0.14	0.32 ± 0.08	14.38 ± 11.75	–	52.34 ± 0.19	–
κ Cet	RGS1	5.61	2.93 ± 0.13	1.12 ± 0.09	0.22 ± 0.05	–	50.54 ± 0.07	–
μ Vel	MEG	123.40	2.29 ± 0.13	0.45 ± 0.08	1.35 ± 0.67	1.23 ± 0.35	51.33 ± 0.31	52.04 ± 0.10
	HEG	146.45	–	–	–	2.36 ± 0.91	–	52.28 ± 0.13
π^1 UMa	RGS1	2.56	1.43 ± 0.08	0.51 ± 0.05	0.24 ± 0.07	–	50.59 ± 0.08	–
Procyon	LETG	0.49	2.05 ± 0.08	3.06 ± 0.12	0.10 ± 0.01	–	50.14 ± 0.03	–
Prox Cen	MEG	0.03	2.19 ± 0.22	0.76 ± 0.17	–	–	48.67 ± 0.12	49.25 ± 0.14
	HEG	0.03	–	–	–	–	–	49.24 ± 0.35
Speedy Mic	MEG	223.00	1.26 ± 0.13	0.20 ± 0.07	1.25 ± 1.36	1.66 ± 0.65	51.17 ± 0.22	52.16 ± 0.14
	HEG	–40	–	–	–	1.36 ± 1.40	–	51.89 ± 0.47
V471 Tau	LETG	112.34	1.46 ± 0.09	0.30 ± 0.06	1.85 ± 1.06	–	51.39 ± 0.20	–
VW Cep	LETG	70.42	3.74 ± 0.13	0.83 ± 0.09	1.62 ± 0.46	–	51.37 ± 0.10	–
ξ UMa	MEG	14.87	11.45 ± 0.40	3.43 ± 0.28	0.59 ± 0.13	0.64 ± 0.07	50.99 ± 0.14	51.75 ± 0.04
	HEG	16.45	–	–	–	0.60 ± 0.14	–	51.72 ± 0.08
YY Gem	LETG	37.12	7.06 ± 0.23	1.93 ± 0.15	1.07 ± 0.24	–	51.25 ± 0.07	–
YZ CMi	RGS1	3.30	5.48 ± 0.21	1.99 ± 0.13	0.16 ± 0.03	–	50.41 ± 0.09	–

[a] At $T = 2$ MK. [b] At $T = 4$ MK.

Table A.2. Measured line counts for O VII and Ne IX intercombination (i) and forbidden (f) lines, corresponding f/i ratios (corrected for $A_{\rm eff}$), and plasma densities $n_{\rm e}$ derived from Eq. (2). All errors are 1 σ errors.

		O VII				Ne IX			
Star	Instr.	i [cts]	f [cts]	f/i	log($n_{\rm e}$)	i [cts]	f [cts]	f/i	log($n_{\rm e}$)
24 UMa	MEG	2.55 ± 1.97	14.52 ± 4.00	6.37 ± 5.22	<11.9	18.84 ± 5.70	80.49 ± 10.10	4.69 ± 1.53	<11.8
	HEG	–	–	–	–	8.83 ± 3.32	13.64 ± 3.99	1.61 ± 0.77	11.8 ± 0.42
44 Boo	MEG	32.92 ± 6.46	49.79 ± 7.70	1.69 ± 0.42	10.6 ± 0.19	132.90 ± 15.01	352.56 ± 25.21	2.91 ± 0.39	11.0 ± 0.52
	HEG	–	–	–	–	40.76 ± 7.17	84.48 ± 10.46	2.17 ± 0.47	11.5 ± 0.27
47 Cas	RGS1	55.19 ± 12.64	105.41 ± 14.67	2.00 ± 0.54	10.5 ± 0.24	–	–	–	–
AB Dor	RGS1	230.94 ± 24.70	407.50 ± 27.21	1.83 ± 0.23	10.5 ± 0.10	–	–	–	–
	MEG	15.60 ± 5.02	36.98 ± 6.75	2.65 ± 0.98	10.2 ± 0.74	137.61 ± 13.53	290.84 ± 18.73	2.32 ± 0.27	11.4 ± 0.16
	HEG	–	–	–	–	33.50 ± 6.11	77.68 ± 9.19	2.42 ± 0.53	11.4 ± 0.37
α Cen A	LETG	38.41 ± 6.99	109.60 ± 11.06	2.82 ± 0.59	10.1 ± 0.39	–	–	–	–
α Cen B	RGS1	20.34 ± 6.49	111.23 ± 11.60	5.68 ± 1.91	<10.2	–	–	–	–
	LETG	36.09 ± 7.09	154.54 ± 13.06	4.23 ± 0.90	<10.8	–	–	–	–
AD Leo	RGS1	166.09 ± 17.75	356.13 ± 22.02	2.23 ± 0.27	10.4 ± 0.12	–	–	–	–
	LETG	53.01 ± 9.21	170.31 ± 14.52	3.17 ± 0.61	9.92 ± 0.74	–	–	–	–
	MEG	18.56 ± 4.45	30.68 ± 5.65	1.85 ± 0.56	10.5 ± 0.25	53.71 ± 7.85	171.40 ± 14.05	3.50 ± 0.59	<12.0
	HEG	–	–	–	–	12.77 ± 3.61	26.91 ± 5.26	2.20 ± 0.76	11.5 ± 0.50
Algol	RGS1	104.99 ± 25.25	90.89 ± 24.58	0.90 ± 0.33	10.6 ± 1.41	–	–	–	–
	LETG	186.85 ± 22.27	184.01 ± 22.30	0.97 ± 0.17	10.4 ± 0.47	–	–	–	–
	MEG	51.46 ± 8.54	31.58 ± 7.29	0.69 ± 0.19	10.9 ± 0.29	150.82 ± 15.43	236.96 ± 18.28	1.72 ± 0.22	11.7 ± 0.11
	HEG	–	–	–	–	35.73 ± 6.99	53.05 ± 8.12	1.55 ± 0.39	11.8 ± 0.20
AT Mic	RGS1	134.91 ± 17.58	238.57 ± 18.83	1.84 ± 0.28	10.5 ± 0.12	–	–	–	–
AU Mic	RGS1	209.47 ± 21.95	688.37 ± 31.28	3.44 ± 0.39	9.70 ± 0.67	–	–	–	–
	MEG	10.05 ± 3.52	45.99 ± 6.97	5.11 ± 1.95	<10.9	78.25 ± 9.95	214.19 ± 15.80	3.00 ± 0.44	10.9 ± 1.00
	HEG	–	–	–	–	24.99 ± 5.08	52.33 ± 7.29	2.19 ± 0.54	11.5 ± 0.32
β Cet	RGS1	19.48 ± 8.40	79.44 ± 11.74	4.23 ± 1.93	<11.3	–	–	–	–
	LETG	58.12 ± 16.27	178.69 ± 20.17	3.03 ± 0.92	<11.0	–	–	–	–
	MEG	5.49 ± 3.00	23.61 ± 5.25	4.80 ± 2.83	<11.5	127.79 ± 14.00	211.92 ± 17.14	1.82 ± 0.25	11.7 ± 0.12
	HEG	–	–	–	–	32.41 ± 6.07	64.72 ± 8.30	2.09 ± 0.47	11.6 ± 0.26
Canopus	MEG	1.20 ± 1.41	13.42 ± 3.87	12.47 ± 15.09	–	23.29 ± 5.74	42.20 ± 7.13	1.99 ± 0.59	11.6 ± 0.33
	HEG	–	–	–	–	4.68 ± 2.28	13.03 ± 3.66	2.91 ± 1.64	<12.0
χ^1 Ori	RGS1	22.27 ± 8.18	123.42 ± 13.40	5.75 ± 2.20	<10.5	–	–	–	–
EK Dra	RGS1	30.25 ± 8.06	59.68 ± 9.82	2.05 ± 0.64	10.4 ± 0.29	–	–	–	–
	LETG	23.82 ± 7.19	31.03 ± 7.53	1.29 ± 0.50	10.8 ± 0.28	–	–	–	–
ϵ Eri	RGS1	41.69 ± 8.90	160.21 ± 14.34	3.99 ± 0.92	<10.9	–	–	–	–
	LETG	153.61 ± 14.85	453.99 ± 22.78	2.92 ± 0.32	10.0 ± 0.20	–	–	–	–
EQ Peg	RGS1	46.25 ± 9.95	142.72 ± 13.99	3.20 ± 0.76	<10.8	–	–	–	–
ER Vul	MEG	4.14 ± 3.03	18.06 ± 5.05	4.88 ± 3.83	<11.9	51.41 ± 9.56	168.72 ± 14.75	3.60 ± 0.74	<12.1
	HEG	–	–	–	–	16.96 ± 4.53	32.71 ± 6.17	2.02 ± 0.66	11.6 ± 0.37
EV Lac	RGS1	128.92 ± 16.34	291.00 ± 20.31	2.34 ± 0.34	10.3 ± 0.16	–	–	–	–
	MEG	40.31 ± 6.59	54.92 ± 7.58	1.52 ± 0.33	10.7 ± 0.15	85.95 ± 10.78	222.32 ± 16.34	2.84 ± 0.41	11.1 ± 0.48
	HEG	–	–	–	–	24.32 ± 5.20	68.82 ± 8.55	2.96 ± 0.73	<12.0
HD 223460	MEG	10.64 ± 3.89	7.37 ± 3.36	0.77 ± 0.45	11.1 ± 0.43	–	–	–	–
κ Cet	RGS1	63.15 ± 11.60	153.99 ± 15.00	2.55 ± 0.53	10.2 ± 0.28	–	–	–	–
μ Vel	MEG	4.26 ± 2.96	27.60 ± 5.73	7.24 ± 5.24	<11.5	50.20 ± 8.94	59.62 ± 9.23	1.30 ± 0.31	11.9 ± 0.17
	HEG	–	–	–	–	24.12 ± 5.49	31.65 ± 5.93	1.37 ± 0.40	11.9 ± 0.22
π^1 UMa	RGS1	30.39 ± 8.22	94.81 ± 11.76	3.24 ± 0.96	<10.8	–	–	–	–
Procyon	LETG	203.00 ± 16.80	652.40 ± 27.40	3.17 ± 0.29	9.90 ± 0.25	–	–	–	–
Prox Cen	MEG	5.73 ± 2.45	18.19 ± 4.33	3.55 ± 1.74	<10.5	5.54 ± 2.89	18.02 ± 5.03	3.57 ± 2.11	<12.9
	HEG	–	–	–	–	2.93 ± 1.73	12.81 ± 4.92	4.57 ± 3.22	<12.9
Speedy Mic	MEG	3.75 ± 2.22	8.56 ± 3.14	2.55 ± 1.77	<11.2	11.57 ± 3.68	37.35 ± 6.82	3.54 ± 1.30	<12.5
	HEG	–	–	–	–	2.77 ± 1.74	10.59 ± 3.32	3.99 ± 2.80	<13.0
V471 Tau	LETG	16.11 ± 7.37	43.43 ± 9.19	2.66 ± 1.34	<11.2	–	–	–	–
VW Cep	LETG	72.06 ± 12.18	89.71 ± 12.90	1.23 ± 0.27	10.8 ± 0.15	–	–	–	–
ξ UMa	MEG	39.15 ± 6.40	72.85 ± 8.65	2.08 ± 0.42	10.4 ± 0.19	138.57 ± 13.41	354.90 ± 20.13	2.81 ± 0.32	11.1 ± 0.31
	HEG	–	–	–	–	29.59 ± 5.73	81.17 ± 9.20	2.87 ± 0.64	<12.1
YY Gem	LETG	50.64 ± 9.63	115.75 ± 12.44	2.26 ± 0.49	10.4 ± 0.23	–	–	–	–
YZ CMi	RGS1	88.70 ± 13.07	169.54 ± 15.80	2.00 ± 0.35	10.5 ± 0.15	–	–	–	–

Table A.3. Derived volumes $V_{\rm cor}$ in comparison with available volumes $V_{\rm avail}$.

		O VII			Ne IX		
Star	Instr.	$\log V^a_{\rm cor}$ [cm^3]	$\log V^b_{\rm av}$ [cm^3]	f^c %	$\log V^a_{\rm cor}$ [cm^3]	$\log V^b_{\rm av}$ [cm^3]	f^c %
24 UMa	MEG	29.4	33.2	0.01	30.8	33.4	0.22
	HEG	–	–	–	28.5	32.2	0.02
44 Boo	MEG	30.0	32.9	0.11	30.1	32.6	0.38
	HEG	–	–	–	29.0	32.0	0.11
47 Cas	RGS1	30.5	33.5	0.09	–	–	–
AB Dor	RGS1	30.3	33.0	0.16	–	–	–
	MEG	30.7	33.4	0.18	29.4	32.2	0.18
	HEG	–	–	–	29.5	32.2	0.23
α Cen A	LETG	28.7	31.4	0.18	–	–	–
α Cen B	RGS1	31.2	33.5	0.51	–	–	–
	LETG	29.4	31.6	0.62	–	–	–
AD Leo	RGS1	29.8	33.5	0.01	–	–	–
	LETG	30.7	32.6	1.08	–	–	–
	MEG	29.2	31.9	0.19	29.1	31.5	0.43
	HEG	–	–	–	28.1	30.8	0.20
Algol	RGS1	30.4	34.0	0.02	–	–	–
	LETG	31.0	34.3	0.05	–	–	–
	MEG	30.0	33.7	0.02	29.1	32.8	0.02
	HEG	–	–	–	28.9	32.7	0.01
AT Mic	RGS1	30.1	32.5	0.37	–	–	–
AU Mic	RGS1	31.8	34.2	0.35	–	–	–
	MEG	31.0	34.3	0.04	29.1	31.7	0.28
	HEG	–	–	–	28.7	31.3	0.24
β Cet	RGS1	31.1	34.1	0.10	–	–	–
	LETG	30.8	34.5	0.01	–	–	–
	MEG	30.5	33.1	0.22	29.1	32.9	0.01
	HEG	–	–	–	29.4	33.0	0.02
Canopus	MEG	–	–	–	29.7	33.5	0.01
	HEG	–	–	–	29.0	33.1	0.00
χ^1 Ori	RGS1	31.5	33.3	1.48	–	–	–
EK Dra	RGS1	30.4	33.1	0.21	–	–	–
	LETG	29.7	32.9	0.06	–	–	–
ϵ Eri	RGS1	30.2	32.1	1.43	–	–	–
	LETG	30.1	32.3	0.62	–	–	–
EQ Peg	RGS1	30.2	32.3	0.84	–	–	–
ER Vul	MEG	29.8	33.3	0.02	30.5	33.1	0.28
	HEG	–	–	–	29.4	32.5	0.07
EV Lac	RGS1	29.8	32.1	0.48	–	–	–
	MEG	28.9	33.0	0.00	28.9	31.3	0.38
	HEG	–	–	–	28.1	30.8	0.19
HD 223460	MEG	30.2	33.4	0.05	–	–	–
κ Cet	RGS1	30.1	32.6	0.33	–	–	–
μ Vel	MEG	30.4	34.8	0.00	28.1	32.3	0.00
	HEG	–	–	–	28.4	32.4	0.01
π^1 UMa	RGS1	29.9	32.2	0.50	–	–	–
Procyon	LETG	30.4	32.3	1.31	–	–	–
Prox Cen	MEG	27.6	32.9	0.00	25.5	28.7	0.06
	HEG	–	–	–	25.4	28.7	0.05
Speedy Mic	MEG	29.0	29.9	11.5	29.2	32.4	0.05
	HEG	–	–	–	27.8	31.6	0.01
V471 Tau	LETG	29.8	32.9	0.08	–	–	–
VW Cep	LETG	29.7	32.8	0.08	–	–	–
ξ UMa	MEG	30.1	34.1	0.01	29.6	32.1	0.30
	HEG	–	–	–	28.8	31.7	0.10
YY Gem	LETG	30.5	33.0	0.31	–	–	–
YZ CMi	RGS1	29.5	31.9	0.36	–	–	–

[a]Emitting coronal volumes from Eq. (4). [b]Available volumes from Eq. (7).
[c]Filling factor $f = V_{\rm cor}/V_{\rm avail}$.

Table A.4. Same as Table A.1 for RS CVn systems in our sample.

		L_X	Line flux (10^{-13} erg cm^{-2} s^{-1})		$L_{X,O\,VII}$	$L_{X,Ne\,IX}$	log(EM/cm^{-3})	
Star	Instr.	[10^{28} erg/s]	O VIII	O VII(r)	[10^{28} erg/s]	[10^{28} erg/s]	O VII[a]	Ne IX[b]
AR Lac	RGS1	627.14	9.35 ± 0.28	1.15 ± 0.12	4.59 ± 1.50	–	51.88 ± 0.10	–
	MEG	514.49	7.39 ± 0.48	0.80 ± 0.23	2.34 ± 3.31	10.31 ± 2.31	–	52.87 ± 0.09
	HEG	415.12	–	–	–	7.62 ± 4.18	–	52.88 ± 0.17
Capella	RGS1	145.38	28.64 ± 0.36	9.96 ± 0.23	3.54 ± 0.22	–	–	–
	LETG	186.56	30.56 ± 0.25	8.87 ± 0.16	3.33 ± 0.16	–	51.74 ± 0.02	–
	MEG	153.08	30.89 ± 0.44	8.15 ± 0.29	3.24 ± 0.30	2.67 ± 0.16	51.71 ± 0.14	52.37 ± 0.02
	HEG	127.43	–	–	–	2.91 ± 0.31	–	52.39 ± 0.04
HR 1099	RGS1	432.49	16.22 ± 0.40	2.72 ± 0.20	5.40 ± 1.15	–	51.93 ± 0.05	–
	LETG	973.74	24.54 ± 0.35	2.84 ± 0.17	5.09 ± 0.88	–	51.95 ± 0.05	–
	MEG	1000.85	28.99 ± 0.56	3.42 ± 0.27	5.98 ± 1.41	13.44 ± 1.07	52.03 ± 0.09	53.11 ± 0.03
	HEG	798.38	–	–	–	16.25 ± 2.12	–	53.20 ± 0.04
II Peg	MEG	1318.60	19.90 ± 0.68	1.54 ± 0.28	10.43 ± 4.29	19.72 ± 2.71	52.01 ± 0.25	53.26 ± 0.05
	HEG	1045.50	–	–	–	12.80 ± 4.19	–	53.02 ± 0.12
IM Peg	MEG	2520.70	3.37 ± 0.19	0.28 ± 0.08	6.38 ± 6.84	19.34 ± 4.41	51.98 ± 0.07	53.20 ± 0.08
	HEG	2316.90	–	–	–	20.76 ± 8.66	–	53.25 ± 0.14
λ And	RGS1	249.61	12.12 ± 0.31	1.67 ± 0.14	2.21 ± 0.61	–	51.62 ± 0.07	–
	LETG	935.90	23.22 ± 0.35	2.25 ± 0.17	3.38 ± 0.77	–	51.75 ± 0.07	–
	MEG	198.33	10.74 ± 0.36	1.41 ± 0.18	1.93 ± 0.75	3.51 ± 0.51	51.54 ± 0.17	52.55 ± 0.05
	HEG	121.17	–	–	–	1.92 ± 0.73	–	52.22 ± 0.13
σ^2 CrB	RGS1	322.59	20.56 ± 0.52	3.23 ± 0.25	3.24 ± 0.76	–	51.75 ± 0.09	–
	MEG	305.60	19.17 ± 0.47	2.59 ± 0.23	3.25 ± 0.75	5.78 ± 0.54	51.66 ± 0.16	52.73 ± 0.03
	HEG	154.81	–	–	–	5.73 ± 1.00	–	52.68 ± 0.06
TY Pyx	MEG	532.60	3.64 ± 0.27	0.73 ± 0.16	4.64 ± 3.35	8.64 ± 2.34	51.93 ± 0.08	52.93 ± 0.09
	HEG	550.70	–	–	–	7.19 ± 4.54	–	52.78 ± 0.21
UX Ari	RGS1	953.03	13.85 ± 0.34	1.59 ± 0.15	7.80 ± 2.51	–	52.17 ± 0.07	–
	LETG	1306.36	12.62 ± 0.23	1.57 ± 0.12	9.15 ± 1.91	–	52.17 ± 0.07	–
	MEG	804.46	10.36 ± 0.46	1.69 ± 0.25	8.31 ± 4.07	21.45 ± 3.09	52.20 ± 0.39	53.26 ± 0.05
	HEG	502.40	–	–	–	8.87 ± 4.10	–	52.97 ± 0.15
V824 Ara	MEG	254.66	8.63 ± 0.30	1.02 ± 0.14	2.39 ± 0.92	5.44 ± 0.72	51.57 ± 0.21	52.67 ± 0.05
	HEG	212.00	–	–	–	5.49 ± 1.34	–	52.72 ± 0.08
VY Ari	RGS1	366.79	7.66 ± 0.24	1.22 ± 0.12	5.62 ± 1.55	–	51.94 ± 0.09	–

[a] At $T = 2$ MK. [b] At $T = 4$ MK.

Table A.5. Same as Table A.2 for RS CVn systems in our sample.

		O VII				Ne IX			
star	Instr.	i [cts]	f [cts]	f/i	$\log(n_e)$	i [cts]	f [cts]	f/i	$\log(n_e)$
AR Lac	RGS1	48.70 ± 14.75	110.15 ± 16.82	2.35 ± 0.80	10.3 ± 0.42	–	–	–	–
	MEG	1.60 ± 2.58	3.80 ± 2.86	2.65 ± 4.71	–	48.98 ± 8.38	140.80 ± 13.32	3.15 ± 0.62	<11.8
	HEG	–	–	–	–	10.09 ± 3.67	13.90 ± 4.23	1.44 ± 0.68	11.9 ± 0.40
Capella	RGS1	339.67 ± 30.84	1618.64 ± 48.15	4.95 ± 0.47	–	–	–	–	–
	LETG	645.44 ± 33.14	2348.32 ± 53.78	3.59 ± 0.20	9.51 ± 0.40	–	–	–	–
	MEG	167.92 ± 13.94	505.48 ± 23.16	3.36 ± 0.32	9.76 ± 0.38	709.92 ± 32.20	1373.17 ± 42.87	2.12 ± 0.12	11.5 ± 0.06
	HEG	–	–	–	–	190.47 ± 14.76	373.48 ± 20.09	2.05 ± 0.19	11.6 ± 0.10
HR 1099	RGS1	82.61 ± 19.30	254.27 ± 23.89	3.20 ± 0.80	<10.9	–	–	–	–
	LETG	114.78 ± 18.72	254.79 ± 22.49	2.19 ± 0.41	10.4 ± 0.18	–	–	–	–
	MEG	36.05 ± 8.90	93.87 ± 11.80	2.91 ± 0.81	10.0 ± 0.75	304.42 ± 24.39	834.17 ± 34.81	3.01 ± 0.27	10.9 ± 0.38
	HEG	–	–	–	–	100.55 ± 11.62	228.75 ± 16.25	2.38 ± 0.32	11.4 ± 0.20
II Peg	MEG	33.61 ± 6.95	44.83 ± 7.82	1.49 ± 0.40	10.7 ± 0.20	103.95 ± 13.27	268.87 ± 18.85	2.84 ± 0.41	11.1 ± 0.48
	HEG	–	–	–	–	19.99 ± 4.55	46.00 ± 6.95	2.41 ± 0.66	11.4 ± 0.50
IM Peg	MEG	4.46 ± 3.49	10.70 ± 4.16	2.68 ± 2.34	<11.2	49.64 ± 9.16	127.99 ± 13.33	2.83 ± 0.60	11.1 ± 1.05
	HEG	–	–	–	–	12.86 ± 4.01	30.64 ± 5.83	2.49 ± 0.91	11.3 ± 1.14
λ And	RGS1	39.10 ± 15.08	131.08 ± 17.88	3.48 ± 1.42	<10.6	–	–	–	–
	LETG	72.16 ± 21.57	259.98 ± 26.03	3.56 ± 1.12	<10.5	–	–	–	–
	MEG	11.47 ± 4.64	33.55 ± 6.64	3.27 ± 1.47	<10.8	81.33 ± 11.89	219.34 ± 17.80	2.96 ± 0.49	11.0 ± 1.12
	HEG	–	–	–	–	12.84 ± 3.92	35.64 ± 6.22	2.90 ± 1.02	<12.0
σ^2 CrB	RGS1	61.46 ± 15.44	173.44 ± 20.53	2.93 ± 0.81	10.0 ± 0.80	–	–	–	–
	MEG	50.90 ± 7.91	94.28 ± 10.29	2.07 ± 0.39	10.4 ± 0.17	296.10 ± 20.73	521.80 ± 26.92	1.93 ± 0.17	11.6 ± 0.08
	HEG	–	–	–	–	88.11 ± 9.85	130.60 ± 11.74	1.55 ± 0.22	11.8 ± 0.11
TY Pyx	MEG	6.52 ± 2.82	7.52 ± 2.98	1.29 ± 0.76	10.8 ± 0.49	26.51 ± 7.03	72.69 ± 9.73	3.01 ± 0.89	<11.9
	HEG	–	–	–	–	7.09 ± 3.13	16.96 ± 4.54	2.50 ± 1.29	<12.3
UX Ari	RGS1	30.31 ± 15.89	117.54 ± 18.79	4.03 ± 2.21	<11.5	–	–	–	–
	LETG	53.55 ± 14.68	227.42 ± 20.40	4.19 ± 1.21	<11.0	–	–	–	–
	MEG	7.02 ± 3.76	20.91 ± 5.42	3.33 ± 1.98	<10.8	120.16 ± 12.36	237.38 ± 17.32	2.17 ± 0.27	11.5 ± 0.15
	HEG	–	–	–	–	7.99 ± 3.23	18.57 ± 4.60	2.43 ± 1.15	<12.4
V824 Ara	MEG	22.35 ± 5.24	30.23 ± 6.02	1.51 ± 0.46	10.7 ± 0.23	157.09 ± 15.50	298.00 ± 19.26	2.08 ± 0.25	11.6 ± 0.13
	HEG	–	–	–	–	29.84 ± 5.90	66.01 ± 8.44	2.31 ± 0.54	11.4 ± 0.35
VY Ari	RGS1	52.58 ± 14.52	144.81 ± 17.34	2.86 ± 0.86	10.1 ± 0.79	–	–	–	–

Table A.6. Same as Table A.3 for RS CVn systems in our sample.

		O VII			Ne IX		
Star	Instr.	$\log V^a_{\rm cor}$ [cm^3]	$\log V^b_{\rm av}$ [cm^3]	f^c %	$\log V^a_{\rm cor}$ [cm^3]	$\log V^b_{\rm av}$ [cm^3]	f^c %
AR Lac	RGS1	31.3	33.0	1.78	–	–	–
	MEG	–	–	–	30.3	33.2	0.13
	HEG	–	–	–	29.1	32.5	0.04
Capella	LETG	32.8	35.0	0.64	–	–	–
	MEG	32.3	34.9	0.26	29.3	32.9	0.02
	HEG	–	–	–	29.2	32.8	0.02
HR 1099	RGS1	31.3	34.1	0.19	–	–	–
	LETG	31.2	34.2	0.08	–	–	–
	MEG	32.0	32.7	18.8	31.4	33.8	0.40
	HEG	–	–	–	30.4	33.2	0.17
II Peg	MEG	30.6	34.3	0.02	31.1	33.6	0.32
	HEG	–	–	–	30.3	33.2	0.10
IM Peg	MEG	29.0	33.5	0.00	30.2	33.8	0.02
	HEG	–	–	–	29.6	33.4	0.01
λ And	RGS1	30.7	33.9	0.06	–	–	–
	LETG	31.2	34.5	0.04	–	–	–
	MEG	30.4	34.4	0.01	29.9	33.0	0.08
	HEG	–	–	–	28.9	32.5	0.02
σ^2 CrB	RGS1	31.7	34.1	0.37	–	–	–
	MEG	30.8	33.4	0.23	29.5	32.5	0.08
	HEG	–	–	–	29.0	32.1	0.08
TY Pyx	MEG	30.3	33.5	0.07	29.8	32.9	0.08
	HEG	–	–	–	28.7	32.5	0.01
UX Ari	RGS1	31.1	34.1	0.08	–	–	–
	LETG	32.2	34.8	0.25	–	–	–
	MEG	30.7	33.4	0.17	30.2	33.1	0.13
	HEG	–	–	–	29.0	32.5	0.03
V824 Ara	MEG	30.2	33.7	0.03	29.5	32.6	0.08
	HEG	–	–	–	29.9	32.7	0.15
VY Ari	RGS1	31.8	34.3	0.34	–	–	–

[a]Emitting coronal volumes from Eq. (4). [b]Available volumes from Eq. (7).
[c]Filling factor $f = V_{\rm cor}/V_{\rm avail}$.